

Note: This is the originally submitted version and may contain errors/changes that were revised during peer review. Please refer to the final published version for the authoritative version of the article.

This is the original submission version (pre-peer review) of the following article:

Mathew, A. T., Feliu-Talegon, D., Abdullahi Adamu, Y., ben Hmida, I., Armanini, C., Stefanini, C., Seneviratne, L., & Renda, F. (2025). ZodiAq: An Isotropic Flagella-Inspired Soft Underwater Drone for Safe Marine Exploration. *Soft Robotics*, which has now been formally published in final form at *Soft Robotics* at <https://doi.org/10.1089/soro.2024.0036>.

This original submission version of the article may be used for non-commercial purposes in accordance with the Mary Ann Liebert, Inc., publishers' self-archiving terms and conditions.

ZodiAq: An Isotropic Flagella-Inspired Soft Underwater Drone for Safe Marine Exploration

Anup Teejo Mathew^{1*}, Daniel Feliu-Talegon¹, Yusuf Abdullahi Adamu¹,
Ikhlal Ben Hmida¹, Costanza Armanini², Cesare Stefanini³,
Lakmal Seneviratne⁴, Federico Renda^{1,4}

¹Department of Mechanical Engineering, Khalifa University, Abu Dhabi, UAE.

²Center for Artificial Intelligence and Robotics (CAIR),
New York University, Abu Dhabi, UAE

³Department of Excellence in Robotics and AI, The Biorobotics Institute,
Scuola Superiore Sant'Anna, Pisa 56127, Italy

⁴Khalifa University Center for Autonomous Robotic Systems (KUCARS),
Khalifa University, Abu Dhabi, UAE

*Corresponding author: anup.mathew@ku.ac.ae

March 26, 2025

Keywords: underwater soft robot, modeling and control, biologically-inspired robots, mechatronics

Abstract: The inherent challenges of robotic underwater exploration, such as hydrodynamic effects, the complexity of dynamic coupling, and the necessity for sensitive interaction with marine life, call for the adoption of soft robotic approaches in marine exploration. To address this, we present a novel prototype, ZodiAq, a soft underwater drone inspired by prokaryotic bacterial flagella. ZodiAq's unique dodecahedral structure, equipped with 12 flagella-like arms, ensures design redundancy and compliance, ideal for navigating complex underwater terrains. The prototype features a central unit based on a Raspberry Pi, connected to a sensory system for inertial, depth, and vision detection, and an acoustic modem for communication. Combined with the implemented control law, it renders ZodiAq an intelligent system. This paper details the design and fabrication process of ZodiAq, highlighting design choices and prototype capabilities. Based on the strain-based modeling of Cosserat rods, we have developed a digital twin of the prototype within a simulation toolbox to ease analysis and control. To optimize its operation in dynamic aquatic conditions, a simplified model-based controller has been developed and implemented, facilitating intelligent and adaptive

movement in the hydrodynamic environment. Extensive experimental demonstrations highlight the drone’s potential, showcasing its design redundancy, embodied intelligence, crawling gait, and practical applications in diverse underwater settings. This research contributes significantly to the field of underwater soft robotics, offering a promising new avenue for safe, efficient, and environmentally conscious underwater exploration.

1 Introduction

Our vast ocean, covering more than 70% of the Earth’s surface, is a realm of unparalleled potential and critical environmental concern. These waters, teeming with diverse ecosystems, are vital not only for marine life but also for the health of the planet and the well-being of billions of people. In this context, the development and deployment of unmanned underwater Remotely Operated Vehicles (ROVs) are of immense significance. While there exist several industrial solutions for tasks such as environmental monitoring and resource mapping [1], the closeup exploration of underwater life and navigation near cluttered seabeds or around submerged structures demand bio-inspired designs that can prevent unintended impacts with the delicate marine environment [2]. The high-frequency rotation of traditional motors close to the sea floor or marine life can cause self-damage and disturb marine life, making it harder to study underwater ecosystems.

Compared to their rigid counterparts, the compliant nature of soft robots allows for safer, less precision-demanding, bio-compatible, and adaptable interactions with unpredictable environments. Inspired by the efficient morphology and body structure of aquatic organisms, soft roboticists have proposed a range of bio-inspired designs for different swimming strategies [3, 4, 5, 6]. Lift-powered swimming, inspired by the techniques of animals such as manta rays [7] and turtles [8], utilizes hydrodynamic lift forces generated by the movement of their fins or limbs. The undulation strategy, in contrast, relies on the body’s wave-like motion, effectively producing propulsion thrust through the cyclical storage and release of elastic energy. Robot designs in this category draw inspiration from the slender and streamlined bodies of creatures like snakes [9], and eels [10], making them ideal for navigating narrow environments. Animals such as fishes, frogs, and insects utilize limb movements reminiscent of oars, pushing water backward to generate forward thrust from the resulting reaction force. This drag-powered swimming gait is characterized by its agility and reduced turning radius and has been adapted in various robotic designs [2, 11, 12]. Lastly, the jet propulsion strategy, used by animals like squids and octopi, propels them forward by expelling water, utilizing the conservation of momentum principle [13, 14].

Most soft robot designs, inspired by the aforementioned locomotion strategies, require intricate mechanisms or the incorporation of smart materials. This contrasts with the simpler, conventional motor-based propellers used in rigid underwater vehicles. Recently, a novel macroscale underwater locomotion strategy has been developed in a high Reynolds number regime, combining motor rotary actuation with an elongated passive soft filament acting as the rotor [15]. The strategy mimics the swimming gait of bacterial flagella, often regarded as the only example of a biological “wheel.” The transmitted torque and external fluid interaction on the soft body prompt the soft body to adopt a helical shape, effectively generating the propulsion thrust needed for

movement [16, 17]. Unlike traditional (rigid) propellers that depend on high-frequency, low-torque rotation, these macroscale soft propellers utilize low-frequency, high-torque actuation, offering a powerful yet biocompatible mode of locomotion. In a previous work [18], we presented a comprehensive design, characterization, and modeling framework of flagellate underwater robots. The flagella were modeled using the strain-based modeling approach of Cosserat rods [19, 20], while simplifying assumptions are used to model fluid interaction forces due to buoyancy, drag, lift, and added mass.

Underwater drones used for close inspection of marine environments can benefit from a compact turning radius and the ability to maneuver in all three dimensions. Designing with redundancy is beneficial, allowing the drone to remain functional even if some components fail, greatly improving its reliability in complex underwater settings. Accounting for all these functionalities, we introduce a new design for a soft robot comprising 12 flagella modules arranged symmetrically across a dodecahedral shell. We named it “ZodiAq” to signify its characteristic shape with 12 actuators, with ‘Aq’ indicating its aquatic nature. The design and fabrication details of the prototype are provided in Section 2.

To analyze locomotion and develop control laws, we created a digital twin of ZodiAq using SoRoSim, a MATLAB toolbox based on the Geometric Variable Strain (GVS) model [21]. The methodology for constructing the digital twin and a sample simulation result are described in Section 3. We have developed a simplified model-based control law and implemented it on the digital twin to control all 6 DoFs of the robot body, while for the prototype, control of depth and orientation is achieved. Details of the control law, simulation, and experimental results are described in Section 4.

Using four experimental demonstrations (Section 5), we showcase the capabilities of ZodiAq and their real-world applications. Our first demonstration focuses on the design redundancy of ZodiAq, which ensures that the prototype remains functional even with the failure of an actuator module. In the second demonstration, we explored ZodiAq’s ‘Embodied Intelligence,’ derived from its soft body’s physical form (compliance) [22, 23]. This built-in intelligence facilitates seamless interaction with the environment, minimizing control needs and optimizing the use of environmental features. The third demonstration is dedicated to showing another locomotion gait of the prototype: crawling. Finally, the fourth demonstration highlights ZodiAq’s ability to navigate artificial coral, showcasing its suitability for close inspection tasks in marine settings. The final section (Section 6) provides conclusive remarks on the results presented in this work and outlines potential future developments of the proposed system.

2 Design and Fabrication

To achieve omnidirectional movement and rotation about the vertical axis, as well as to ensure design redundancy, we opted to equip the robot with 12 flagella modules. For geometrical symmetry, we chose a dodecahedron – the fourth Platonic solid – as the shell structure of the robot (Figure 1A). Each pentagonal face of the robot houses a motor canister assembly to power the flagella, which are fabricated through a silicone molding process with a 3D-printed hook embedded at their base. ZodiAq utilizes a Raspberry Pi to control the angular speed

and direction of each DC motor. The sensory system of ZodiAq consists of a camera for vision, sensors including a temperature and humidity sensor for internal damage detection, an Inertial Measurement Unit (IMU) for motion detection, a depth sensor for depth feedback, and an acoustic modem for underwater communication. The entire system is powered by Lithium Polymer (LiPo) batteries, which are mounted inside. Lastly, a ballast is mounted inside to shift the center of gravity below the center of buoyancy. A comprehensive list of all external and internal components of ZodiAq are listed in Table 1.

[Figure 1 about here.]

[Table 1 about here.]

The schematic of the electrical connection is shown in Figure 1B. The charging and operation circuits are split into two: one for the Raspberry Pi and another for the motor drivers. The setup includes components for short-circuit protection, voltage balancing, and voltage conversion. The motors associated with the 12 flagella modules follow a numbering scheme mentioned in Figure 1C. Pairs of consecutive motors (1 and 2, 3 and 4, etc.) are arranged on opposite sides of the prototype. This particular arrangement ensures minimum load on the motor drivers and assists in simplifying the control law (details in the Supplementary Material).

The components are methodically arranged on two internal racks: the lower rack houses batteries and ballasts, while the Raspberry Pi and its peripherals are mounted on the upper rack. The mass of all the internal components is balanced against the water mass of the displaced volume of the ZodiAq's shell. The mass distribution and balancing results in the prototype's neutral and stable buoyancy. The fully assembled ZodiAq prototype, immersed underwater, is shown in Figure 1D.

We tested the prototype's functionality up to a depth of 2.5 meters and an estimated operational duration of 1 hour, constrained primarily by Raspberry Pi's energy consumption. The neutral stability of the prototype is validated in an experiment illustrated in Figure 1D. In this test, a vertical force (f_a) was applied to a side-mounted motor canister, causing the prototype to descend and tilt. The force (f_b) and the stabilizing moment (m_b) due to buoyancy successfully repositioned the prototype, restoring its height and orientation. Readers may refer to the video demonstration in the supplementary movie S1. Table 2 lists the key specifications of the prototype. For detailed information on the design and fabrication, readers may refer to the supplementary material.

[Table 2 about here.]

3 Digital Twin of ZodiAq

To analyze the dynamics and formulate control laws, we created a digital twin of ZodiAq using the SoRoSim toolbox. The toolbox was developed based on the Geometric Variable Strain (GVS) approach, offering a unified mathematical framework for modeling soft and rigid bodies [21]. The GVS approach is based on the strain-parameterization of the Cosserat rod: a 1D continuum mechanics object with axial torsion, bending

in two directions, axial stretch, and shear in two directions. A summary of the GVS model is provided in the supplementary material, while for a detailed review, the readers may refer to [19, 20]. The versatility of SoRoSim allows for the analysis of open-, closed-, and branched hybrid robots in various external load and actuation conditions, making it ideal for modeling ZodiAq.

The toolbox defines links and their assembly, linkages, as MATLAB class objects. Each link has a rigid joint and a soft or rigid body. The geometric and material properties of the link are defined during link creation. For the robot’s dodecahedral shell, we created a rigid link with a 6 DoF free joint. Shafts are created as rigid links with revolute joints and assembled appropriately using a fixed transformation matrix \mathbf{g}_f (Figure 2A) corresponding to each face of the shell. Connected to each shaft is a hook, a rigid link with a fixed joint (0 DoF) and a pre-curvature, and to each hook we connect a flagellum, a soft link with a fixed joint. We model the soft flagellum as an inextensible Kirchhoff rod, a sub-class of Cosserat rod with torsion and bending with linear strain parameterization (6 DoFs). The total number of links in the linkage (assembly) is 37 and the total DoFs of the system are 90. The linkage creation also allows users to define external forces and actuators. External forces due to gravity and fluid interaction including buoyancy, drag, lift, and added mass (fluid displacement) are considered. Joints of the shafts are defined as actuators that are controlled by joint angles. Finally, a simplified control law, discussed in the next section, is implemented. The overview of the linkage creation in SoRoSim is shown in Figure 2B. For a comprehensive understanding, readers may refer to the supplementary material.

[Figure 2 about here.]

Analysis of dynamic response is a ‘method’ of the linkage class object. For an illustrative simulation, we arbitrarily actuated motors M6, M8, M9, and M11, which are distributed predominantly on one side of the dodecahedral shell, at 60 RPM in the CCW direction (Figure 2C). We noted that besides the intended straight-line motion towards the opposite side (-ve x-axis), there was an unintended drift of $0.74m$ in the y-axis and a minor displacement of $0.03m$ meters in the z-axis. Additionally, the robot experienced a significant orientation shift about the z-axis by 32.8° . The deployment of controllers, which will be discussed in the subsequent section, could aid in sustaining precise orientation and trajectory during movement. The dynamic simulation video is available for viewing in the supplementary movie S2. Readers can also simulate the digital twin in MATLAB through the GitHub link provided in [24].

4 Nonlinear Motion Control for Robot Navigation

The dynamic modeling of our robot is highly complex, primarily due to the interaction between the soft parts with the fluid. With a total of 90 DoFs and 12 inputs, the dynamics of the robot presents substantial challenges for model-based control design. We propose a simplified model that solely accounts for the robot’s shell. The collective input, or throttle input, is determined by aggregating the forces and moments generated by each flagellum positioned at the center of each face. The proposed model allows, quite realistically, to develop a

nonlinear model-based controller of the system for performing robot navigation. The control law demonstrates the tracking performance in the simplified system's states, encompassing the 3D position and orientation about the vertical axis (ψ) of the shell. The orientation of the remaining two angles stabilizes towards the zero equilibrium point, showcasing the system's inherent stability and highlighting the control over the six DoFs of the main body in simulations. The developed control law has been employed in the complete system dynamics (digital twin), demonstrating the effectiveness of the simplified model for control design. However, due to the absence of a tracking system in our experimental setup, planar coordinates (x and y) feedback is unavailable for the actual prototype. Consequently, our control implemented in the real prototype is limited to depth (z) and orientation about the vertical axis (ψ) while the planar movement (x and y) was controlled in an open-loop manner by commanding a desired acceleration. This adjustment in the control law enables the execution of various trajectories with the actual prototype, including straight-line movements, square paths, and rotational maneuvers, as we demonstrate later on. In the experiments, the depth measurement is directly obtained from the depth sensor, while the orientation angle is derived from the calibrated magnetic field measurements provided by the IMU. The details of the simplified model and the control law are explained in Supplementary Material.

4.1 Closed-Loop Control Simulation

The effectiveness of the proposed control method is tested using the digital twin, which simulates the whole dynamics of the system. The proposed control law predefined the rotation direction of each flagellum, considering that the direction of the rotation does not impact the direction of the thrust. Moreover, it combines the two motors of opposite faces to create a new input, making the system differentially flat. We conduct closed-loop control simulations where the system executes a planar semicircular trajectory with a radius of 2 m over 60 s while also controlling the orientation of the vertical axis ψ and the depth z of the system. Moreover, we can see that the Euler angles ϕ and θ remain stable around the equilibrium point without the need to control those variables directly in the closed loop. The simulation results, together with the developed control scheme, are shown in Figure 3. Readers may watch the supplementary movie S3 for a dynamic simulation of ZodiAq demonstrating semicircular trajectory tracking.

[Figure 3 about here.]

4.2 Depth and Orientation Control

Our preliminary experiment focused on validating the control of height and orientation (Figure 4). The desired orientation and depth were established based on the prototype's initial measurements upon being submerged. Once the robot achieved stability, the prototype's depth and orientation were intentionally altered by applying external forces and moments. The control system responded adeptly to these disturbances, effectively restoring the prototype to its pre-set depth and orientation. Figure 4A demonstrates the depth control: the drone is pushed downward using a rod. Subsequently, using the depth feedback, the control system actively minimizes the depth error and returns the drone to its initial depth. Notably, the buoyancy force also plays a role in facilitating

this correction. Figure 4B illustrates the orientation control: after a forced clockwise rotation of the drone, the control system corrects the induced orientation error, realigning to the initial orientation. Readers can access the supplementary movie S4 to see a video demonstration of height and orientation control, including CW and CCW rotations, as well as vertical shifts downwards and upwards. Figure 4C shows the measured and desired values of orientation angle and depth, while Figure 4D illustrates the output rotational velocities (ω/ω_{max}) of all twelve motors, as determined by the controller. To avoid overloading the motor driver, the velocities have been capped at a magnitude of $0.8\omega_{max}$. The restoring action of the controller can be appreciated from the velocities applied to each motor at different instances of the experiment.

[Figure 4 about here.]

4.3 Square Trajectory

The second experiment aimed to navigate a square trajectory. Due to the absence of planar coordinate feedback in our experimental setup, this method involved maintaining initial orientation and depth while movement along the x- and y-axes are regulated by commanding a desired acceleration. The procedure entailed commanding a positive acceleration in the x-direction and then a positive acceleration in the y-direction. This was followed by commanding a negative acceleration in the x-direction and, finally, a negative acceleration in the y-direction, with each step lasting for 40 seconds.

Figure 5A shows the experimental result of following a square trajectory. Readers may refer to the supplementary movie S5 for the video result. Directions of motion are determined by the initial orientation of the prototype. The prototype successfully follows the square trajectory, except on the fourth side, where a notable deviation is observed. This deviation can be attributed to imperfections in the prototype and the absence of planar coordinates feedback. Additionally, it is important to note that there is no feedback mechanism for planar coordinates. The maximum error in the height is 5 cm (Figure 5B), while the maximum orientation error is 23 degrees (Figure 5C).

[Figure 5 about here.]

5 Experimental Demonstrations

To demonstrate the prototype’s functionalities and potential uses, we delve into experimental demonstrations of design redundancy, embodied intelligence, crawling locomotion, and its application in close exploration of marine environments. Readers may refer to supplementary videos S6 through S9 for video results of these demonstrations.

5.1 Prototype Redundancy

Many factors can lead to the damage of a robotic system as it navigates a complex and unknown terrain. The ability of the robot to accomplish given tasks having lost the functionality of some part, a severed tentacle or

defective motor, for instance, defines the robot’s redundancy. This important feature enhances the adaptability and reliability of the robots that operate in unpredictable underwater environments [25]. The ZodiAq is equipped with 12 actuators specifically to ensure operational redundancy. When an actuator becomes damaged, the robot should redistribute the affected operation among other actuators, significantly lowering the risk of critical failures. To test the redundancy of ZodiAq, we conducted the following experiments (Figure 6).

[Figure 6 about here.]

In the first experiment, ZodiAq was set to move in a straight line in the positive x-direction (acceleration command) with all flagella intact (full system). In the second experiment, we removed one of the actuators (M5), thereby creating an impaired system. As illustrated in Figure 6A, the full system covered a distance of two body lengths every 15 seconds. The impaired system also maintained a straight-line trajectory as depicted in Figure 6B. However, its speed was reduced to one body length every 15 seconds, nearly half the velocity achieved by the full system. It’s important to note that the initial orientation and depth were established at the time of ZodiAq’s placement, resulting in a different x-axis direction for each experiment. From the plot of controlled motor speed against time, the variations in motor speed for both cases can be inferred. Figures 6C and D provide insights into the depth (z) and orientation (ψ) of the robot throughout the experiment. Despite the impairment, the system successfully maintained the measured depth and orientation close to the desired values.

5.2 Embodied Intelligence

In recent times, compliant structures that are capable of using the environment to their advantage rather than avoiding them are getting attention from the soft robotics community [22, 23]. This is in response to the need for robot platforms that can safely interact in complex and dynamic surroundings, especially through embodied cognition [26]. Here, we demonstrate ZodiAq’s ability to navigate through an artificially created environment. The envisaged scenario is depicted in Figure 7A, where the robot is commanded to follow a simple translation along the x-axis. Along the trajectory, an inclined obstruction is placed. The experiment aims to observe the strategy employed by this robot to intentionally interact and utilize the obstacle for its navigation. This approach contrasts the traditional strategy of mapping the environment and using advanced control algorithms to circumvent obstacles [27].

[Figure 7 about here.]

Figure 7B shows the result of the experimental demonstration. The ZodiAq meets the rigid barrier at the 37-second mark. The robot’s arm flexibility enables a safe and advantageous interaction, guiding movement along the barrier. Post-barrier, the ZodiAq resumes its intended path. Notably, at 70 seconds, the flagella presses against a cylindrical block, and at 78 seconds, against the wall’s far edge, utilizing these interactions for forward thrust.

5.3 Crawling Gait

In previous demonstrations, the locomotion of ZodiAq is achieved through the thrust generated by the flagella interacting with the surrounding fluid. Another form of propulsion is possible for this prototype: crawling. Crawling using appendages refers to a mode of locomotion where a robot moves using its limbs to push the body forward [28, 29, 30]. Even though the prototype is not designed for crawling, we made it heavy enough to sink to the floor by increasing the ballast mass. Inspired by the movement of sea turtles, we implemented a manual open-loop actuation strategy (Figure 8A). To propel forward, the left bottom arms (M6 and M8) were rotated CCW, while the right side arms (M10 and M12) were rotated CW. All other actuators were kept passive.

[Figure 8 about here.]

Figure 8B shows the crawling locomotion of ZodiAq. The arms perform a sweeping action that pushes the body forward. Additionally, the robot utilizes the environment, specifically the cylindrical obstacle, to aid its movement. We note that the locomotion cannot be classified as pure crawling, as it is also augmented by thrust from fluid interactions.

5.4 Marine Exploration

Our final demonstration focuses on the application of the prototype for close inspection of a marine environment like that of a coral reef (Figure 9). This scenario establishes a rocky underwater environment simulating a coral reef. As ZodiAq hovers above the target location, a descent command is sent using the acoustic modem. Upon receiving the command, the robot descends and contacts the coral. Despite this contact, it attempts to continue its downward motion. The compliance of the flagella ensures safe interaction with minimal control requirements. Subsequently, a command is sent to rotate the prototype to scan the environment. It can be seen that during the execution of the rotational movement, contact with the environment aids in facilitating the motion.

[Figure 9 about here.]

Figure 9B shows the snapshots taken from the video footage recorded by the onboard camera. In the current prototype, a low-resolution PiCamera module is internally mounted behind a transparent face on one of the top faces. The quality of the footage is also affected by underwater low lighting conditions. This can be enhanced by integrating higher-quality external cameras or floodlights onto the prototype.

6 Discussions and Conclusions

In summary, the paper introduces the design of a novel soft underwater drone featuring a flagella-inspired swimming gait. We have developed a digital twin and a simplified control law to analyze and manage the motion of this complex system. The prototype has demonstrated motion capabilities in 4D: translation along all three axes and rotation about its vertical axis (effectively zero turning radius), which is advantageous for

close inspection tasks. It has shown resilience in operating despite actuator impairments and has engaged in safe interactions with its surroundings, which are beneficial traits in unpredictable marine environments. The prototype demonstrates the ability to effectively utilize the environment to facilitate its motion with minimal control requirements, showcasing the embodied intelligence of its design.

Although the prototype features a range of innovative capabilities, there is scope for improvement in some aspects. The operational redundancy of the robot is constrained by the proposed control law. The control law predefines the rotation direction of the motors and combines the actuators on opposite faces to generate a new input that prevents the simultaneous movement of motors on opposite faces. This constraint is clearly visible in Figure 4D, Figure 6A, and Figure 6B. A fault-tolerant control could be developed for robust navigation to prevent accidents after a motor failure occurs, taking advantage of the system's redundancy property. This opens up the possibility of developing advanced controllers to maintain control and stability in the system, even when failures occur in several defective motors.

While following a square trajectory, it was observed that design imperfections caused deviations in the y direction movement, as illustrated in Figure 5A. These design imperfections can be incorporated into the control law by fine-tuning the thrust and moment vectors of individual actuators. These adjustments enable finer control, allowing the robot to accurately follow intended trajectories despite fabrication errors. Another obvious source of the deviation is the absence of feedback from planar coordinates in the experimental setup. Two or more acoustic modems can be implemented to triangulate the robot and provide planar coordinates feedback.

With these improvements, this prototype holds promise for real-world applications, signaling a significant step forward in the field of soft robotics for underwater exploration. The potential for these technologies to contribute to safe, efficient, and environmentally conscious exploration is immense, and we believe that our work lays a significant step toward realizing this potential.

Acknowledgments

The work was supported by the US Office of Naval Research Global under Grant N62909-21-1-2033 and in part by the Khalifa University of Science and Technology under Grants CIRA-2020-074 and RC1-2018-KUCARS-8474000136.

References

- [1] Petillot YR, Antonelli G, Casalino G, Ferreira F. Underwater Robots: From Remotely Operated Vehicles to Intervention-Autonomous Underwater Vehicles. *IEEE Robotics and Automation Magazine*. 2019;26(2):94–101.
- [2] Katzschmann RK, DelPreto J, MacCurdy R, Rus D. Exploration of underwater life with an acoustically controlled soft robotic fish. *Science Robotics*. 2018;3(16):1–12.

- [3] Aracri S, Giorgio-Serchi F, Suaria G, Sayed ME, Nemitz MP, Mahon S, et al. Soft Robots for Ocean Exploration and Offshore Operations: A Perspective. *Soft Robotics*. 2021;8(6):625–639.
- [4] Li G, Wong TW, Shih B, Guo C, Wang L, Liu J, et al. Bioinspired soft robots for deep-sea exploration. *Nature Communications*. 2023;14(1):1–10.
- [5] Qu J, Xu Y, Li Z, Yu Z, Mao B, Wang Y, et al. Recent Advances on Underwater Soft Robots. *Advanced Intelligent Systems*. 2023;2300299.
- [6] Calisti M, Picardi G, Laschi C. Fundamentals of soft robot locomotion. *Journal of the Royal Society Interface*. 2017;14(130):0–2.
- [7] Chen Z, Um TI, Bart-Smith H. Bio-inspired robotic manta ray powered by ionic polymer-metal composite artificial muscles. *International Journal of Smart and Nano Materials*. 2012;3(4):296–308.
- [8] Kim HJ, Song SH, Ahn SH. A turtle-like swimming robot using a smart soft composite (SSC) structure. *Smart Materials and Structures*. 2013;22(1).
- [9] Kelasidi E, Liljebäck P, Pettersen KY, Grasdahl JT. Innovation in Underwater Robots: Biologically Inspired Swimming Snake Robots. *IEEE Robotics and Automation Magazine*. 2016;23(1):44–62.
- [10] Nguyen DQ, Ho VA. Anguilliform Swimming Performance of an Eel-Inspired Soft Robot. *Soft Robotics*. 2022;9(3):425–439.
- [11] Jia X, Chen Z, Riedel A, Si T, Hamel WR, Zhang M. Energy-Efficient Surface Propulsion Inspired by Whirligig Beetles. *IEEE Transactions on Robotics*. 2015;31(6):1432–1443.
- [12] Marchese AD, Onal Cagdas D, Rus D. Autonomous Soft Robotic Fish Capable of Escape Maneuvers Using Fluidic Elastomer Actuators. *Soft Robotics*. 2014 March;1(1):75–673.
- [13] Godaba H, Li J, Wang Y, Zhu J. A Soft Jellyfish Robot Driven by a Dielectric Elastomer Actuator. *IEEE Robotics and Automation Letters*. 2016;1(2):624–631.
- [14] Giorgio-Serchi F, Arienti A, Laschi C. Underwater soft-bodied pulsed-jet thrusters: Actuator modeling and performance profiling. *International Journal of Robotics Research*. 2016;35(11):1395–1416.
- [15] Calisti M, Giorgio-Serchi F, Stefanini C, Farman M, Hussain I, Armanini C, et al. Design, Modeling and Testing of a Flagellum-inspired Soft Underwater Propeller Exploiting Passive Elasticity. In: 2019 IEEE/RSJ International Conference on Intelligent Robots and Systems (IROS); 2019. p. 3328–3334.
- [16] Yu TS, Lauga E, Hosoi AE. Experimental investigations of elastic tail propulsion at low Reynolds number. *Physics of Fluids*. 2006;18(9).
- [17] Armanini C, Alshehhi AA, Mathew AT, Hmida IB, Stefanini C, Renda F. Model-Based Design Optimization of Underwater Flagellate Propellers. *IEEE Robotics and Automation Letters*. 2022;7(4):10089–10096.

- [18] Armanini C, Farman M, Calisti M, Giorgio-Serchi F, Stefanini C, Renda F. Flagellate Underwater Robotics at Macroscale: Design, Modeling, and Characterization. *IEEE Transactions on Robotics*. 2022;38(2):731–747.
- [19] Renda F, Armanini C, Lebastard V, Candelier F, Boyer F. A Geometric Variable-Strain Approach for Static Modeling of Soft Manipulators With Tendon and Fluidic Actuation. *IEEE Robotics and Automation Letters*. 2020;5(3):4006–4013.
- [20] Boyer F, Lebastard V, Candelier F, Renda F. Dynamics of Continuum and Soft Robots: A Strain Parameterization Based Approach. *IEEE Transactions on Robotics*. 2020;p. 1–17.
- [21] Mathew AT, Hmida IMB, Armanini C, Boyer F, Renda F. SoRoSim: A MATLAB Toolbox for Hybrid Rigid-Soft Robots Based on the Geometric Variable-Strain Approach. *IEEE Robotics and Automation Magazine*. 2022;.
- [22] Pfeifer R, Lungarella M, Iida F. Self-organization, embodiment, and biologically inspired robotics. *Science*. 2007;318(5853):1088–1093.
- [23] Mengaldo G, Renda F, Brunton SL, Bächer M, Calisti M, Duriez C, et al. A concise guide to modelling the physics of embodied intelligence in soft robotics. *Nature Reviews Physics*. 2022;Available from: <https://doi.org/10.1038/s42254-022-00481-z>.
- [24] Ben Hmida I, Feliu-Talegon D, Mathew AT. ZodiAq digital twin in SoRoSim: ZodiAq Branch. *GitHub*. 2024;Available from: <https://github.com/Ikhlal-Ben-Hmida/SoRoSim/tree/ZodiAq>.
- [25] Liu F, Ma Z, Mu B, Duan C, Chen R, Qin Y, et al. Review on fault-tolerant control of unmanned underwater vehicles. *Ocean Engineering*. 2023;285(P2):115471. Available from: <https://doi.org/10.1016/j.oceaneng.2023.115471>.
- [26] Trimmer B. The Artificial Intelligence Revolution: Transforming Robotics for Flexibility and Deformability. *Robotics Reports*. 2024;2(1):29–31.
- [27] Cheng C, Sha Q, He B, Li G. Path planning and obstacle avoidance for AUV: A review. *Ocean Engineering*. 2021;235(July).
- [28] Arienti A, Calisti M, Giorgio-Serchi F, Laschi C. PoseiDRONE: Design of a soft-bodied ROV with crawling, swimming and manipulation ability. In: *Oceans - San Diego, 2013*; 2013. p. 1–7.
- [29] Wu Q, Yang X, Wu Y, Zhou Z, Wang J, Zhang B, et al. A novel underwater bipedal walking soft robot bio-inspired by the coconut octopus. *Bioinspiration and Biomimetics*. 2021;16(4).
- [30] Cianchetti M, Calisti M, Margheri L, Kuba M, Laschi C. Bioinspired locomotion and grasping in water: The soft eight-arm OCTOPUS robot. *Bioinspiration and Biomimetics*. 2015;10(3).

List of Figures

- 1 Prototype Design: (A) CAD model of the prototype (including an exploded view of one face of the prototype), with external components marked in green and internal components in yellow. Components are listed in Table 1, (B) Electrical connection between components, (C) Numbering scheme used for the faces and motors, (C) Fully assembled prototype floating in the water, (E) a Demonstration of passive mechanical stabilization due to neutral and stable buoyancy. A force (f_a) is applied to tilt and push the ZodiAq down. The resulting moment (m_b) due to the arrangement of CB above the CG corrects the tilt as the robot sinks deeper. The force of buoyancy (f_b) restores the height. 17
- 2 (A) Digital twin of the robot, created using SoRoSim toolbox. GC is the Geometric Centre, CM is the Centre of Mass, and \mathbf{g}_f is the transformation matrix from the GC to a motor shaft (M7 in the diagram). (B) A simplified flowchart showing the processes in SoRoSim. (C) Superimposed images of the robot at different time steps during a dynamic simulation. An inset shows a top view (xy-plane) of the motion 18
- 3 Simulated results of the closed-loop system : (A) Schematic illustrating the control strategy implemented in the closed-loop system. The control law aims to simultaneously control the 3D position (x, y, z) and orientation (ψ). The angular speed of the motors, denoted as ω , serves as the system's control input. The output $\mathbf{q} = [\phi, \theta, \psi, x, y, z]^T$ represents the generalized coordinates of the system, while ν represents the output of proportional-derivative (PD) controller. \mathcal{F}_G^* denotes the desired resultant forces and moments applied to the CM, and Ω is the fictitious input that renders the simplified model differentially flat. For a detailed explanation of the simplified model and the proposed control law, readers can refer to the supplementary material. (B) Comparison between reference trajectories and the actual positions of the angular and linear coordinates. (C) 3D representation of the simulation. 19
- 4 Validation of Height and Orientation Control: (A) The sequence of video snapshots illustrates the active depth control by controlling the motors using depth feedback. (B) Process of orientation stabilization using IMU feedback. The direction of the ZodiAq's rotation is shown by green arrows, while the green dot on a face assists in visualizing the orientation throughout the maneuver. (C) Measured angle and depth and their desired values showing controller in action during various experiment instances: pushing down, counterclockwise (CCW) rotation, clockwise (CW) rotation, and pulling up. (D) Controlled motor speed (ω/ω_{max}) vs time. The color of the band represents the value of angular velocity. 20
- 5 Square Trajectory in Open-loop: (A) Superimposed images of the drone attempting to follow a square trajectory in open-loop control. (B) Robot depth measurement obtained from the depth sensor. (C) Orientation about the vertical axis. 21

6	Assessing Design Redundancy: (A) Full system executing a straight-line trajectory. Note that the motors M2, M5, M7, M10, and M12 were most active. (B) The impaired system (after removing flagella attached to M5) attempts the straight-line trajectory. M1 is activated, and M3's activity is increased to compensate for M5's missing flagella. The controller still engaged M5, unaware of the impairment. (C) Comparison of depth measurements for both full and impaired systems. (D) Comparison of orientation measurements for both scenarios	22
7	Demonstration of Soft Interaction and Adaptive Trajectory of the ZodiAq as it follows an open loop straight line motion: (A) Schematics of the scenario. (B) Snapshots of the experimental demonstration capture the robot's soft flagella engaging with a slanted barrier. Contact areas are demarcated with dashed ellipses.	23
8	Demonstration of ZodiAq's crawling gait: (A) To achieve a turtle-like sweeping action, four actuators at the bottom are specifically actuated while keeping all other actuators passive. (B) Crawling locomotion of ZodiAq. Instances of contact with the ground, walls, and a cylindrical obstacle are evident in the video snapshots. Contact regions are demarcated with dashed ellipses. The green dot on a corner assists in visualizing the orientation of ZodiAq.	24
9	Coral reef exploration with ZodiAq: (A) Snapshots of ZodiAq descending towards the coral reef and executing a rotation. The green dot on a corner assists in visualizing the orientation of ZodiAq. (B) Snapshots from the video footage captured by ZodiAq's onboard camera.	25

List of Figures

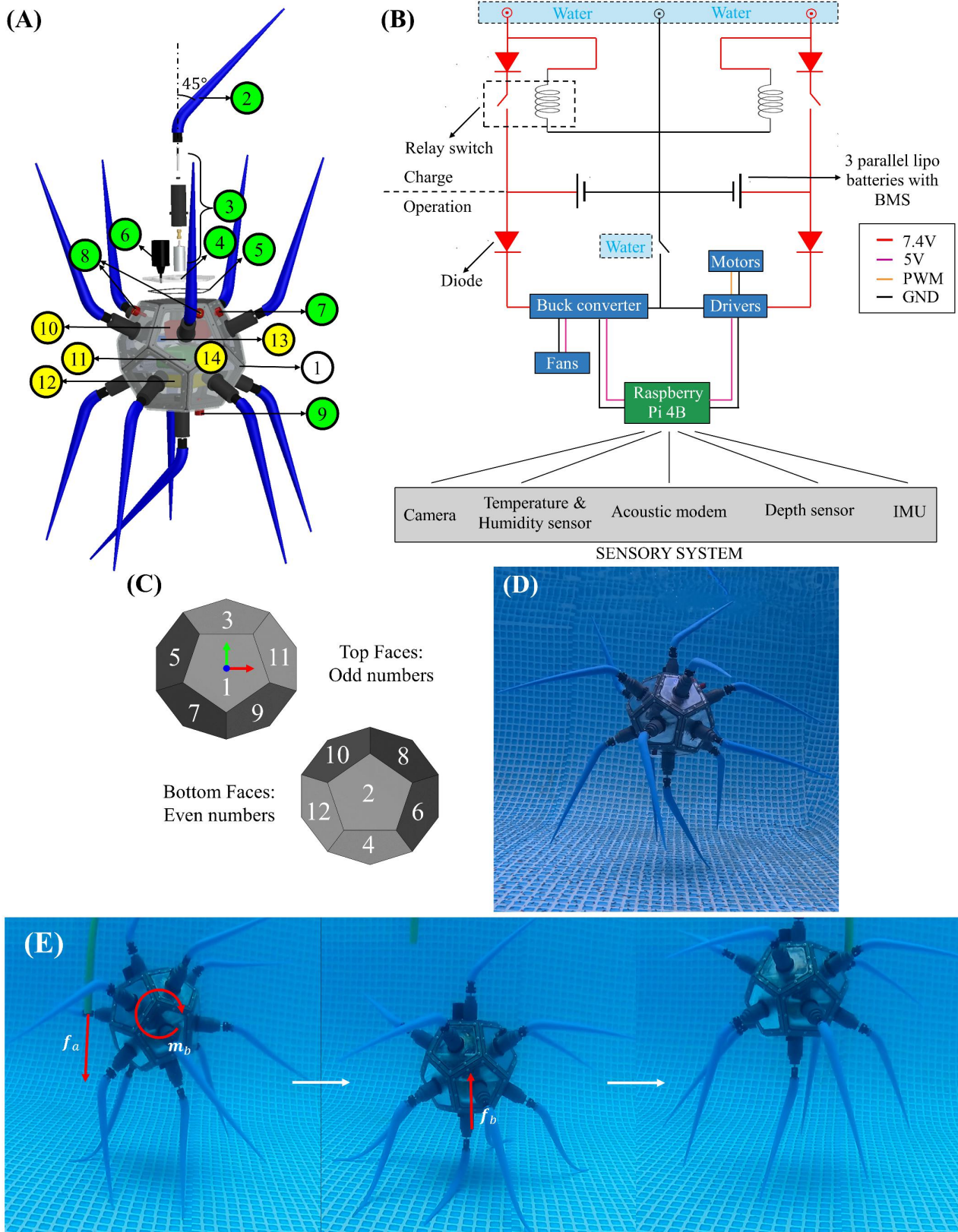


Figure 1: Prototype Design: (A) CAD model of the prototype (including an exploded view of one face of the prototype), with external components marked in green and internal components in yellow. Components are listed in Table 1, (B) Electrical connection between components, (C) Numbering scheme used for the faces and motors, (C) Fully assembled prototype floating in the water, (E) a Demonstration of passive mechanical stabilization due to neutral and stable buoyancy. A force (f_a) is applied to tilt and push the Zodiaq down. The resulting moment (m_b) due to the arrangement of CB above the CG corrects the tilt as the robot sinks deeper. The force of buoyancy (f_b) restores the height.

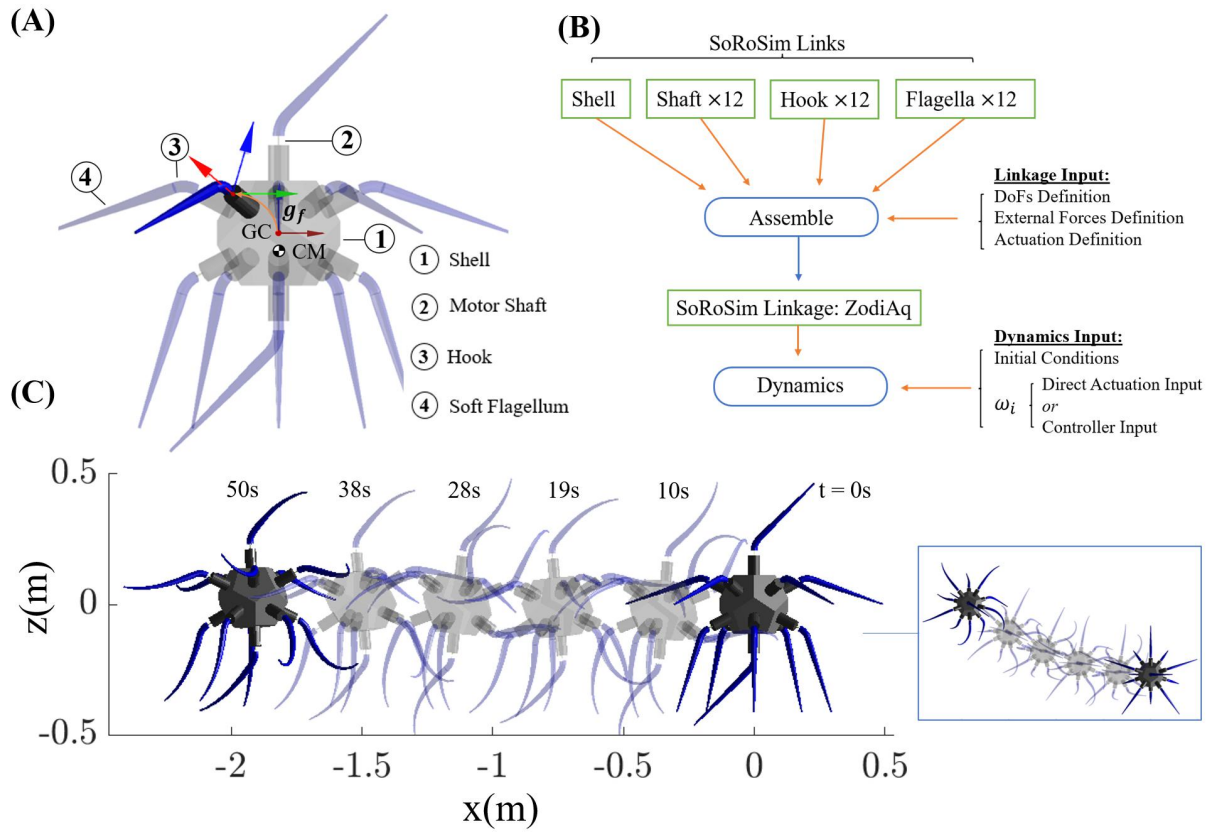


Figure 2: (A) Digital twin of the robot, created using SoRoSim toolbox. GC is the Geometric Centre, CM is the Centre of Mass, and g_f is the transformation matrix from the GC to a motor shaft (M7 in the diagram). (B) A simplified flowchart showing the processes in SoRoSim. (C) Superimposed images of the robot at different time steps during a dynamic simulation. An inset shows a top view (xy-plane) of the motion

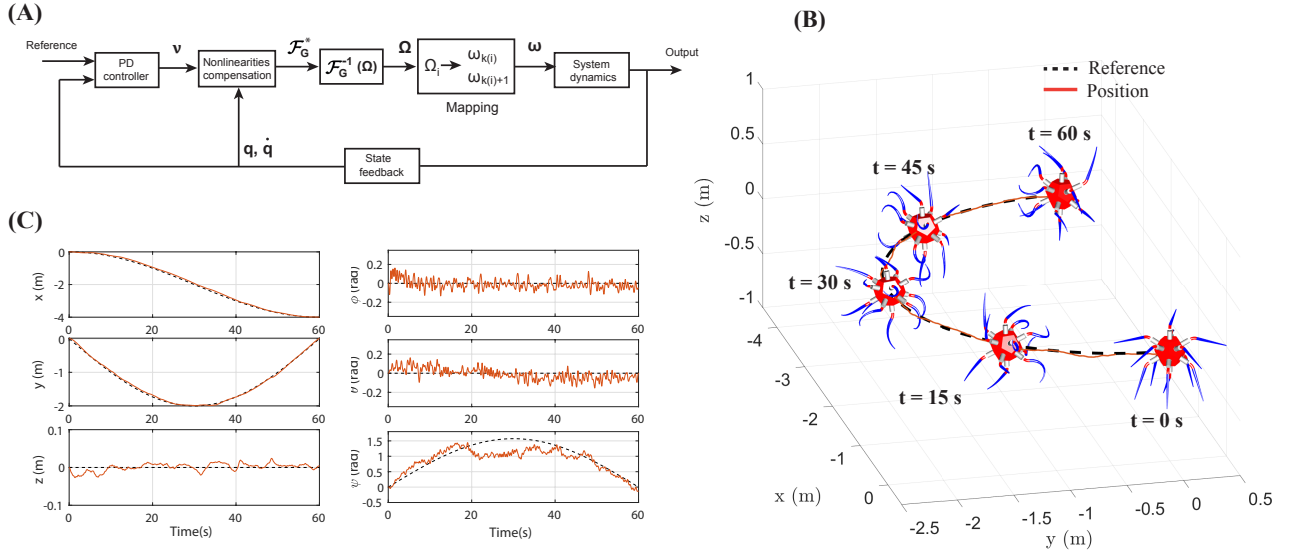


Figure 3: Simulated results of the closed-loop system : (A) Schematic illustrating the control strategy implemented in the closed-loop system. The control law aims to simultaneously control the 3D position (x, y, z) and orientation (ψ) . The angular speed of the motors, denoted as ω , serves as the system's control input. The output $\mathbf{q} = [\phi, \theta, \psi, x, y, z]^T$ represents the generalized coordinates of the system, while \mathbf{v} represents the output of proportional-derivative (PD) controller. \mathcal{F}_G^* denotes the desired resultant forces and moments applied to the CM, and Ω is the fictitious input that renders the simplified model differentially flat. For a detailed explanation of the simplified model and the proposed control law, readers can refer to the supplementary material. (B) Comparison between reference trajectories and the actual positions of the angular and linear coordinates. (C) 3D representation of the simulation.

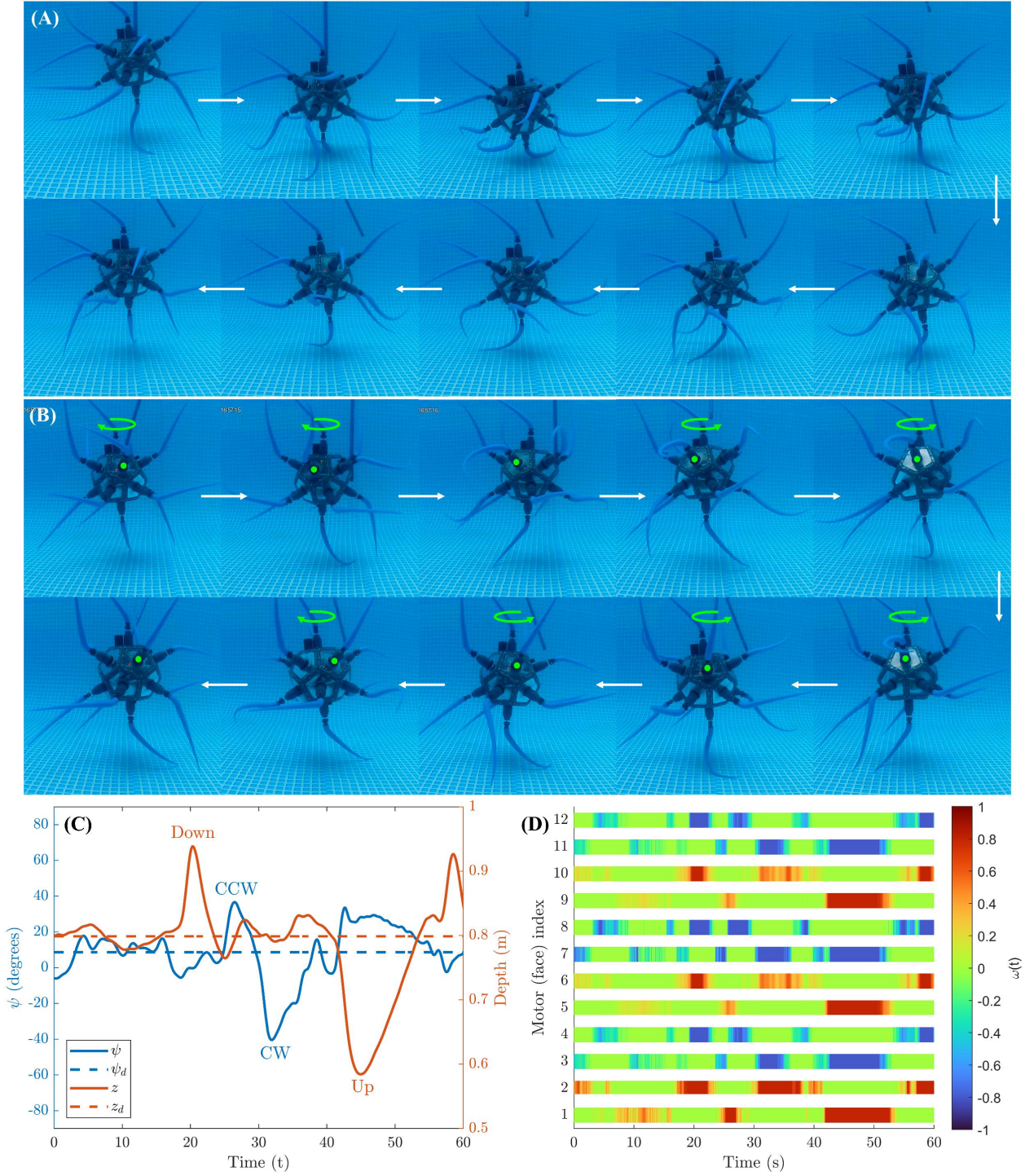


Figure 4: Validation of Height and Orientation Control: (A) The sequence of video snapshots illustrates the active depth control by controlling the motors using depth feedback. (B) Process of orientation stabilization using IMU feedback. The direction of the ZodiAq's rotation is shown by green arrows, while the green dot on a face assists in visualizing the orientation throughout the maneuver. (C) Measured angle and depth and their desired values showing controller in action during various experiment instances: pushing down, counterclockwise (CCW) rotation, clockwise (CW) rotation, and pulling up. (D) Controlled motor speed (ω/ω_{max}) vs time. The color of the band represents the value of angular velocity.

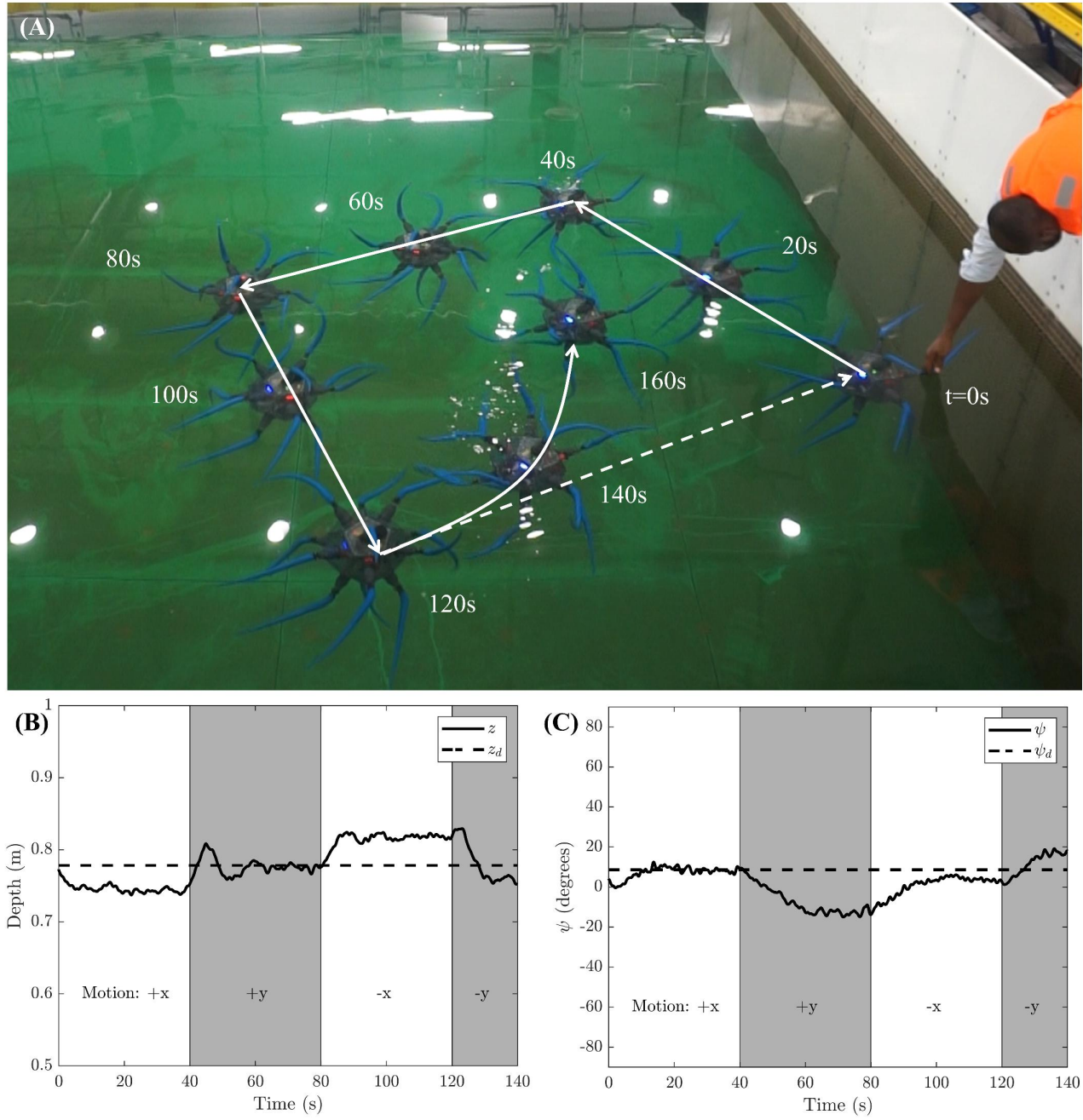


Figure 5: Square Trajectory in Open-loop: (A) Superimposed images of the drone attempting to follow a square trajectory in open-loop control. (B) Robot depth measurement obtained from the depth sensor. (C) Orientation about the vertical axis.

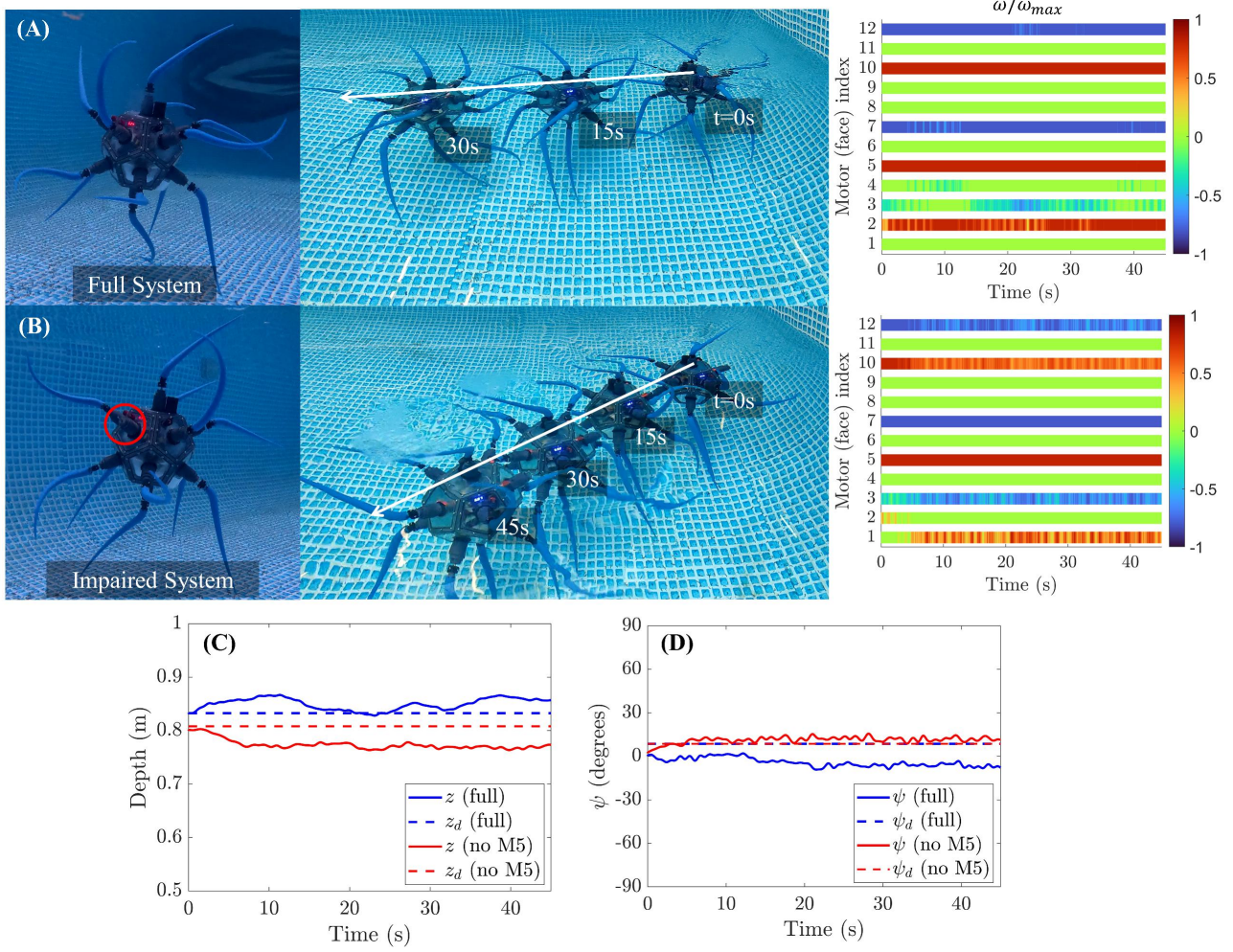


Figure 6: Assessing Design Redundancy: (A) Full system executing a straight-line trajectory. Note that the motors M2, M5, M7, M10, and M12 were most active. (B) The impaired system (after removing flagella attached to M5) attempts the straight-line trajectory. M1 is activated, and M3's activity is increased to compensate for M5's missing flagella. The controller still engaged M5, unaware of the impairment. (C) Comparison of depth measurements for both full and impaired systems. (D) Comparison of orientation measurements for both scenarios

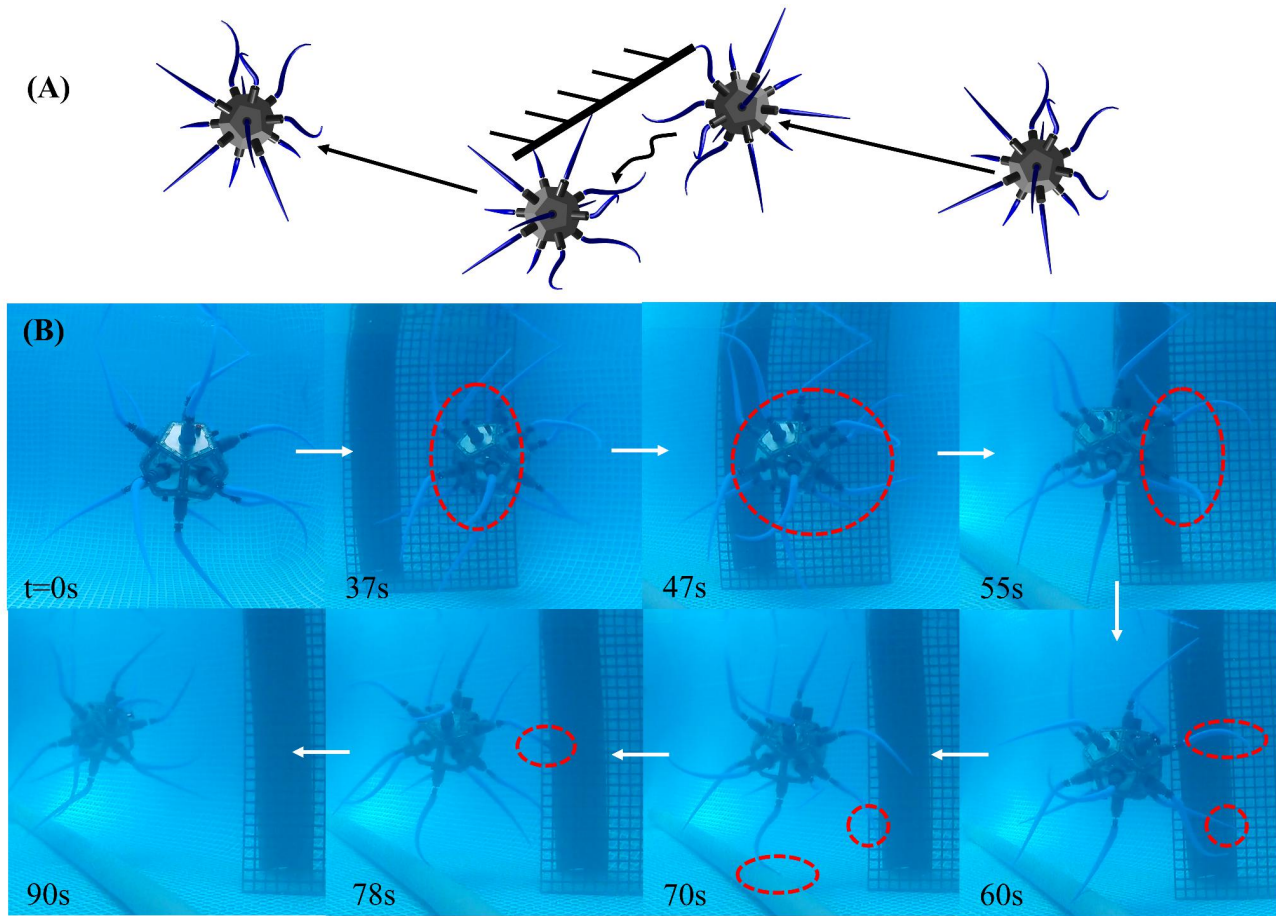


Figure 7: Demonstration of Soft Interaction and Adaptive Trajectory of the ZodiAq as it follows an open loop straight line motion: (A) Schematics of the scenario. (B) Snapshots of the experimental demonstration capture the robot's soft flagella engaging with a slanted barrier. Contact areas are demarcated with dashed ellipses.

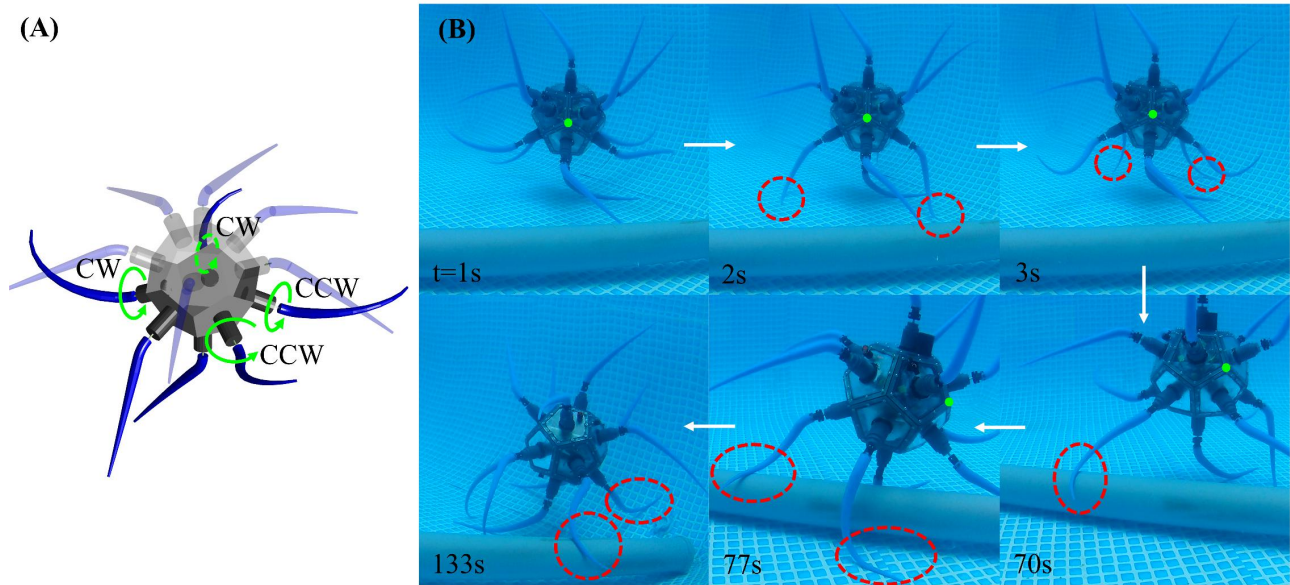


Figure 8: Demonstration of ZodiAq's crawling gait: (A) To achieve a turtle-like sweeping action, four actuators at the bottom are specifically actuated while keeping all other actuators passive. (B) Crawling locomotion of ZodiAq. Instances of contact with the ground, walls, and a cylindrical obstacle are evident in the video snapshots. Contact regions are demarcated with dashed ellipses. The green dot on a corner assists in visualizing the orientation of ZodiAq.

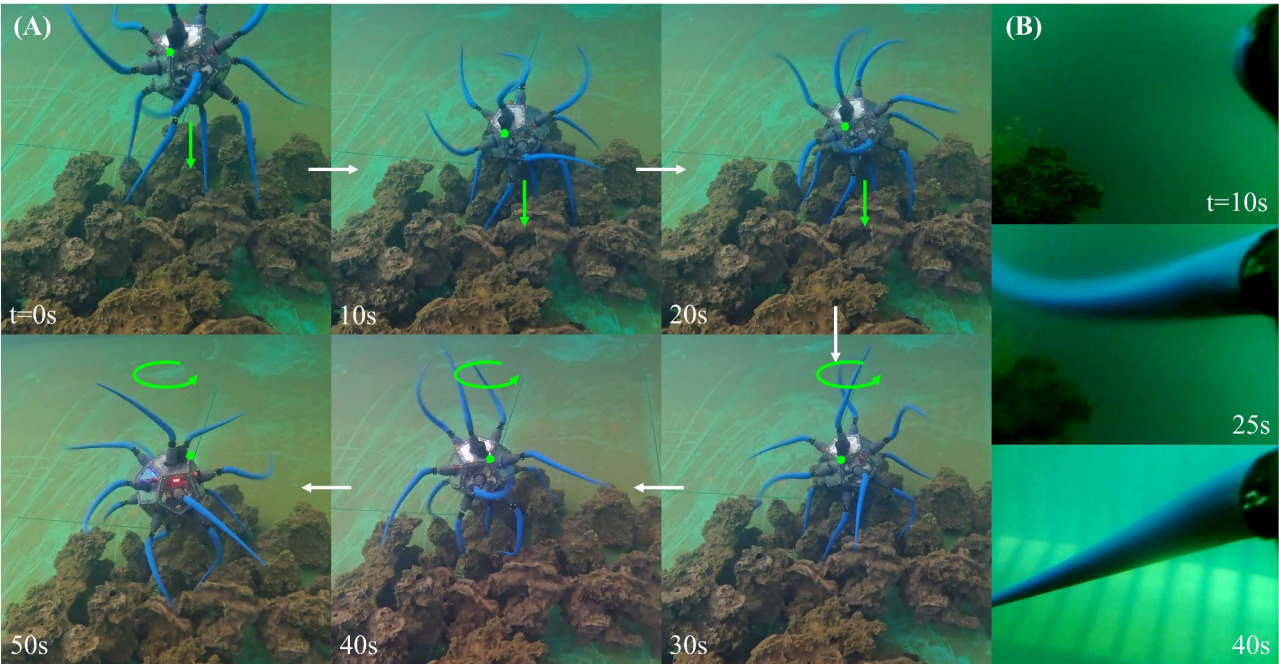


Figure 9: Coral reef exploration with ZodiAq: (A) Snapshots of ZodiAq descending towards the coral reef and executing a rotation. The green dot on a corner assists in visualizing the orientation of ZodiAq. (B) Snapshots from the video footage captured by ZodiAq's onboard camera.

List of Tables

1	Components of ZodiAq according to Figure 1A	27
2	Key specifications of ZodiAq	28

Table 1: Components of ZodiAq according to Figure 1A

Number	Description
1	Dodecahedral frame (PVC) and rack (PLA)
2	Flagella with Hook $\times 12$ (Silicone: Mold Star™ 30)
3	Motor canister assembly ^a $\times 12$
4	Faceplate (Polycarbonate) $\times 12$
5	Face O-rings $\times 12$
6	Acoustic Modem (Succorfish Nanomodem v3)
7	ON/OFF switch
8	Charging ports $\times 2$
9	Depth Sensor
10	Raspberry Pi 4B and accessories ^b
11	Set of three 7.4V 2S Lipo batteries $\times 2$
12	Vinyl coated Lead ballasts (4 kg)
13	Small DC fan $\times 2$
14	Other electrical components ^c

^a Subassembly of DC motor, shaft coupler, shaft, shaft O-rings, and a PVC canister.

^b Adafruit DC motor HATs (Motor drivers) $\times 3$, IMU, Temperature & Humidity sensor, and PiCamera

^c Buck converter (step-down transformer), relay switches, battery management system (BMS), voltage indicators, electrical connections

Table 2: Key specifications of ZodiAq

Property	Value
Edge length of the dodecahedral shell	10 cm
Shell mass	8.57 kg
Total mass	10.75 kg
Downward shift in CG (d_{CG})	3.5 cm
Body Length (BL) (excluding flagella)	30 cm
Maximum operating time	1 hour
Maximum motor speed (ω_{max})	130 RPM
Maximum translational (x-, y-, and z-axis) speed	8 BL /min
Maximum rotational (about z-axis) speed	3π rad/min

Supplementary Materials for ZodiAq: An Isotropic Flagella-Inspired Soft Underwater Drone for Safe Marine Exploration

Anup Teejo Mathew et al.

Corresponding author: anup.mathew@ku.ac.ae

February 21, 2024

1 Details of Design, Fabrication, and Assembly

The development of a soft robot prototype, such as ZodiAq, encompasses several critical stages including the mechanical design, selection of components, fabrication of parts, design, and execution of electrical connections, and assembly. While the summary of the design and fabrication process of the prototype is provided in the manuscript, this section provides details of the process.

1.1 Design and Fabrication of Components

The shell frame of the prototype is constructed from a 9mm thick Polyvinyl Chloride (PVC) sheet. Individual faces of the dodecahedron are machined using a CNC (Computerised Numerical Control) machine and chemically bonded with PVC glue. Two 3D-printed racks are mounted inside the frame to assemble internal components. For the shell's faces, transparent pentagonal sheets made from a 5mm thick polycarbonate are fabricated. Motor canister assemblies are constructed by integrating DC motors, shaft couplers, PVC canisters, and O-rings. We used high torque (0.88 Nm) and low RPM (130 RPM) DC motors. The motor canister assemblies are first adhered to the transparent plates using epoxy glue, followed by a coating of silicone glue. These plates are then fastened to each face of the shell frame, using an O-ring and ten M3 screws to ensure waterproofing. Flagella are manufactured by a molding process using Mold Star™ 30 silicone rubber. A 3D-printed part is inserted into the mold to make the hook area rigid and enable mounting of the flagellum into the motor shaft. Figure 1 explains the fabrication process of these components.

ZodiAq uses a Raspberry Pi 4 Model B as its central unit. The actuators are controlled by the Raspberry Pi through DC motor drivers: Adafruit DC Motor HAT (Hardware Attached on Top), which can control the velocity of four motors in both clockwise and counterclockwise directions using Pulse width modulation (PWM)

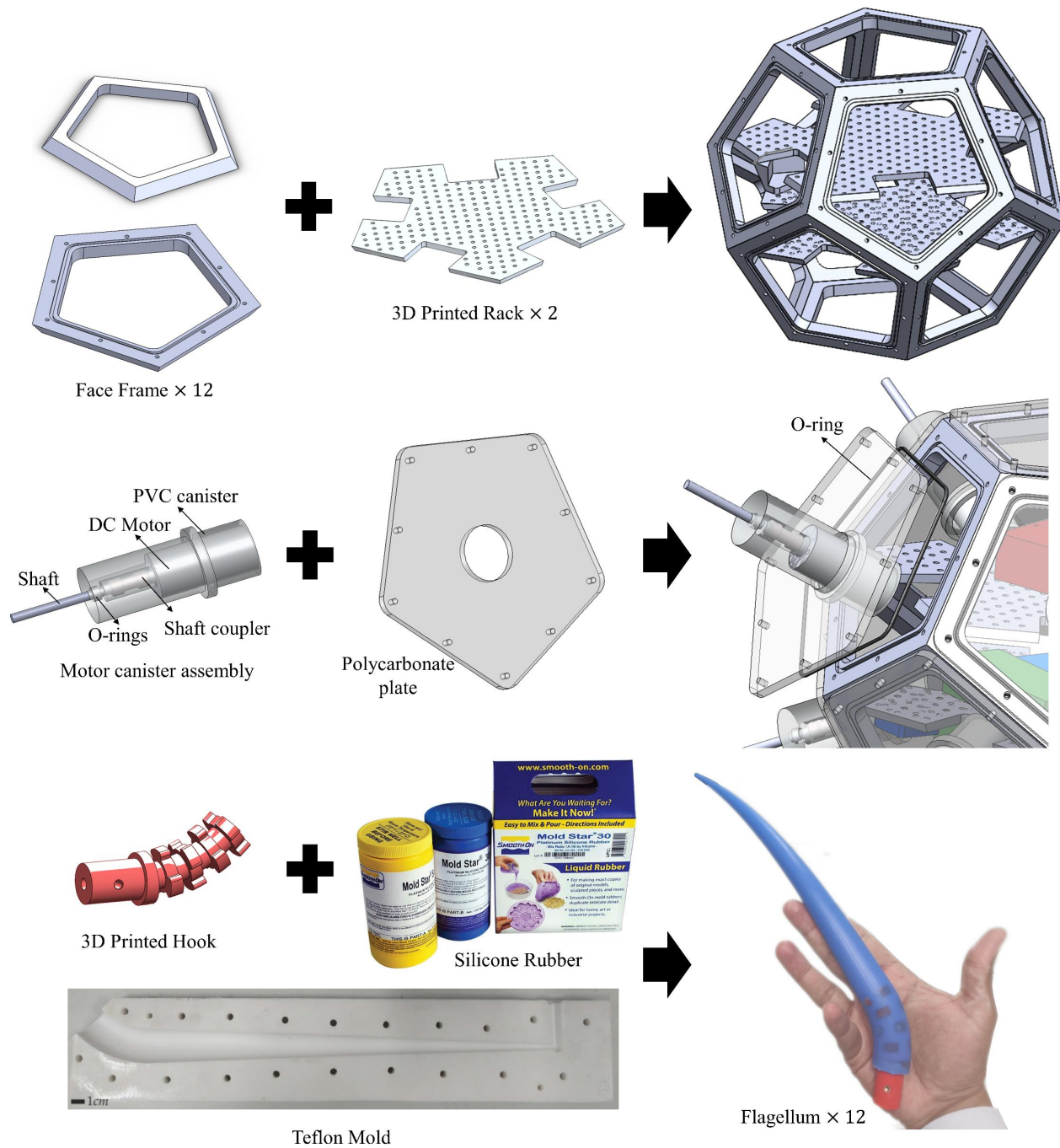


Figure 1: Fabrication of the frame of the dodecahedral shell, motor canister assembly with transparent face plates, and flagellum

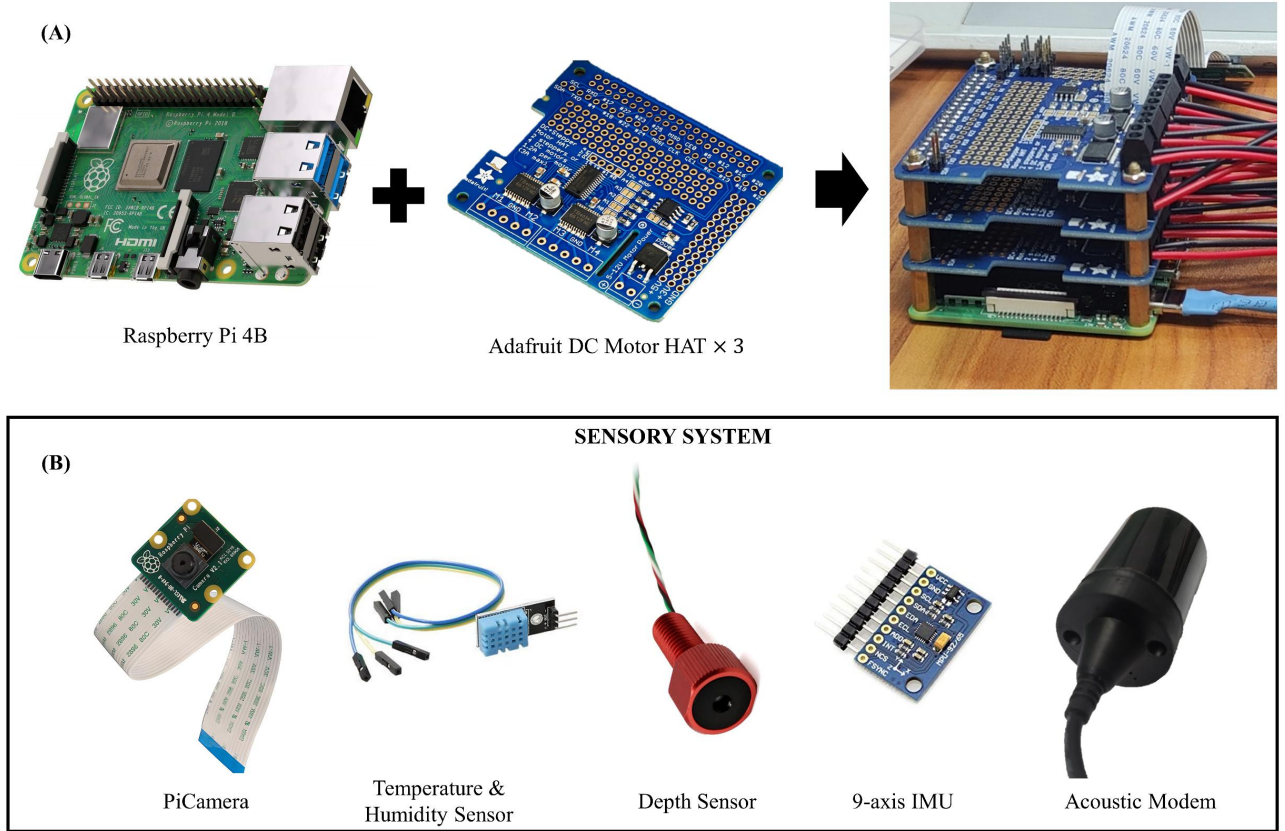


Figure 2: Raspberry Pi and Accessories: (A) Assembly of Raspberry Pi with HATs. (B) Sensory system of ZodiAq

signals. Therefore, to accommodate all 12 motors, three HATs are stacked on the Raspberry Pi (Figure 2A). The sensory system of ZodiAq consists of the following parts. It utilizes the PiCamera, the default camera of the Raspberry Pi, for video capture. The camera is arranged inside, facing outward through one of the transparent faces. For internal monitoring, a temperature and humidity sensor (DHT11) is used to detect any overloading or water leakages. Depth feedback is provided by a depth sensor (MS5837-30BA), and for motion and orientation sensing, a 9-axis Inertial Measurement Unit (MPU-9250) is used. The depth sensor is mounted on the bottom face, while both the IMU and the temperature-humidity sensor are assembled on the top rack. ZodiAq employs an acoustic modem (Succorfish Nanomodem v3) for communication. The modem is attached to the top face using epoxy glue. All these components are connected to the central Raspberry Pi unit, forming the core of ZodiAq's sensory system (Figure 2B).

1.2 Electrical Connections and System Integration

The schematic of the electrical connection of various components of ZodiAq is shown in Figure 1B of the manuscript. The Raspberry Pi and the motors are powered by six 7.4V 2S Lithium Polymer (LiPo) batteries. They are split into two sets, each comprising three batteries connected in parallel. One set powers the Raspberry Pi, while the other operates the HATs which control the motors. Each LiPo battery is connected to a Battery Management System (BMS) for the uniform charging of individual cells. There are two external charging ports available, allowing for the individual charging of each battery set. To prevent short circuits due to the charging

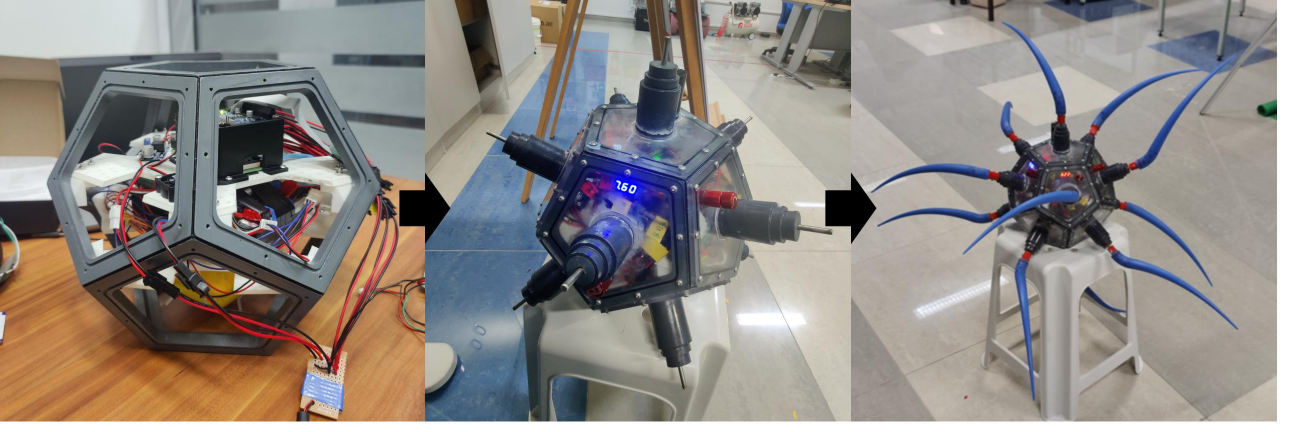


Figure 3: Assembly of ZodiAq

ports being exposed to water, a charging circuit has been designed using a 9V electromagnetic relay switch.

Similarly, the operating circuit is activated using an external waterproof rotary switch. The first set of batteries powers a buck converter, which steps down the voltage from 7.4V to 5V. The output of this converter is then used to power the Raspberry Pi as well as the two internal DC fans, which ensure adequate heat circulation within the shell. ZodiAq's sensory system is connected to the Raspberry Pi via its Camera Serial Interface (PiCamera), digital pins (Temperature-Humidity sensor, depth sensor), I2C interface (IMU), and USB ports (acoustic modem). Meanwhile, the second set of batteries is responsible for powering all three HATs, each connected to four motors: HAT1 to the first four motors, HAT2 to the next four, and HAT3 to the last four. The motor driver, receiving velocity commands from the Raspberry Pi ranging from -1 to 1, generates PWM signals to control motor rotation. Positive and negative command values correspond to clockwise (CW) and counterclockwise (CCW) rotations, respectively, enabling precise speed and directional control.

All internal components are assembled across two racks: batteries on the lower rack and the Raspberry Pi, along with its accessories on the upper rack. A ballast of approximately 4 kg is attached to the lower rack. This strategic placement lowers the center of mass below the center of buoyancy, the geometric center, thereby achieving neutral and stable buoyancy for the prototype. Based on geometric assumptions, we estimate a vertical shift of 3.5 cm. Figure 3 shows the assembly process of the prototype, including the assembly of internal components, faces, and flagella.

2 Mathematical Modeling

2.1 Summary of GVS Model

The GVS model parameterizes the distributed strain field of the Cosserat rod and the joint twists of the rigid joints using basis functions (Φ_{ξ_i}):

$$\xi_i = \Phi_{\xi_i} q_i \quad \text{for rigid joints} \quad (1a)$$

$$\xi_i(X_i) = \Phi_{\xi_i}(X_i) q_i + \xi_i^*(X_i) \quad \text{for soft bodies,} \quad (1b)$$

where ξ_i is the distributed strain field of the i^{th} soft body or the joint twist of the i^{th} rigid link, q_i is the generalized coordinates of the soft body or rigid joint, ξ_i^* is the reference strain field, and $X_i \in [0, 1]$ is the normalized curvilinear abscissa along the centerline of the soft body.

ZodiAq is a branched hybrid system with soft and rigid parts. It consists of a central rigid shell, which is free to translate and rotate in all directions. Protruding from the shell are 12 motor shafts, each modeled as a 1 DoF revolute joint rotating about its local x-axis. The flagella, rigidly connected to each shaft, is composed of two parts: the hook, a rigid body with a 45° pre-curvature, and the soft flagellum. Hence, for the free joint of the shell, $\Phi_{\xi_i} = \mathbf{I}(6)$, for the revolute joints of the shafts, $\Phi_{\xi_i} = [1 \ 0 \ 0 \ 0 \ 0 \ 0]^T$, and for the soft body $\Phi_{\xi_i}(X_i) \in \mathbb{R}^{6 \times n_i}$ is a function of X_i . We model the flagella as an inextensible Kirchhoff rod, a subclass of the Cosserat rod, incorporating torsion and bending. We impose a linear (1st order) strain parameterization, resulting in six degrees of freedom (6 DoFs) per flagellum. The basis function is given by:

$$\Phi_{\xi_i}(X_i) = \begin{bmatrix} 1 & 2X_i - 1 & 0 & 0 & 0 & 0 \\ 0 & 0 & 1 & 2X_i - 1 & 0 & 0 \\ 0 & 0 & 0 & 0 & 1 & 2X_i - 1 \\ 0 & 0 & 0 & 0 & 0 & 0 \\ 0 & 0 & 0 & 0 & 0 & 0 \\ 0 & 0 & 0 & 0 & 0 & 0 \end{bmatrix} \quad (2)$$

The GVS model employs the exponential map of Lie Algebra to compute the forward and differential kinematics of the system, mapping q and $\dot{q} \rightarrow g_i(X_i)$, $J_i(X_i)$, and $\dot{J}_i(X_i)$, where $q \in \mathbb{R}^n$ ($n = \sum n_i$) is the vector of generalized coordinates of the system, encompassing q_i of rigid joints and soft bodies, $g_i \in SE(3)$ is the configuration of i^{th} body with respect to the spatial frame, and $J_i \in \mathbb{R}^{6 \times n}$ is the geometric Jacobian. Projecting the system's free dynamics with the geometric Jacobian through D'Alembert's principle enables the formulation of the generalized dynamic equation of motion in the standard Lagrangian form:

$$M(q)\ddot{q} + (C(q, \dot{q}) + D(q))\dot{q} + Kq = B(q)u + F(q, \dot{q}), \quad (3)$$

where $M(q)$, is the generalized mass matrix, $C(q, \dot{q})$ is the generalized Coriolis matrix, $D(q)$ is the generalized elastic damping matrix, K is the generalized stiffness matrix, $B(q)$ is the generalized actuation matrix, $F(q, \dot{q})$ is the vector of generalized external forces, and u is the vector of applied motor torques.

2.2 Fluid Interaction Forces

The robot experiences external force due to gravity, buoyancy, added mass, drag, and lift forces [1]. For rigid links, external forces are modeled as point wrenches (\mathcal{F}) acting at the geometric center, while for soft links, they are treated as distributed loads ($\bar{\mathcal{F}}$). The subscript i has been intentionally omitted for simplicity. We

have,

$$\mathcal{F} = \mathcal{F}_G + \mathcal{F}_B + \mathcal{F}_D + \mathcal{F}_A \quad (4a)$$

$$\bar{\mathcal{F}} = \bar{\mathcal{F}}_G + \bar{\mathcal{F}}_B + \bar{\mathcal{F}}_D + \bar{\mathcal{F}}_A \quad (4b)$$

The combination of gravity and buoyancy force is given by:

$$\mathcal{F}_G + \mathcal{F}_B = (\mathcal{M} - \rho_w V_{ext} \mathbf{I}_6) \mathcal{G} \quad (5a)$$

$$\bar{\mathcal{F}}_G + \bar{\mathcal{F}}_B = (1 - \rho_w / \rho) \bar{\mathcal{M}} \mathcal{G}, \quad (5b)$$

where, \mathcal{M} is the inertia matrix of a rigid body, $\bar{\mathcal{M}}$ is the linear inertia density of the cross-section of the soft body, ρ is the density of the body, ρ_w is the density of water, and \mathcal{G} is the gravitational acceleration twist expressed in the local frame.

As a body moves underwater, it experiences drag and lift forces due to the interaction with the surrounding fluid. The model of drag and lift force on the bodies are given by:

$$\mathcal{F}_D = -\mathcal{D} \|\nu\| \eta \quad (6a)$$

$$\bar{\mathcal{F}}_D(X) = -\bar{\mathcal{D}}(X) \|\nu(X)\| \eta(X), \quad (6b)$$

where, ν is the translational part of the velocity twist η while, \mathcal{D} and $\bar{\mathcal{D}}$ are the screw matrices of drag and lift coefficients. The form of drag-lift matrix of the shell \mathcal{D}_{shell} , shaft \mathcal{D}_{shaft} , hook $\bar{\mathcal{D}}_h$, and flagellum $\bar{\mathcal{D}}_f$ are given by:

$$\mathcal{D}_{shell} = \frac{1}{2} \rho_w \cdot \text{diag}[C_x A_x R_s^3, C_y A_y R_s^3, C_z A_z R_s^3, C_x A_x, C_y A_y, C_z A_z] \quad (7a)$$

$$\mathcal{D}_{shaft} = \frac{1}{2} \rho_w \cdot \text{diag}[0, 0, 0, C_x A_x, C_y A_y, C_z A_z] \quad (7b)$$

$$\bar{\mathcal{D}}_{h,f}(X) = r_{h,f}(X) \rho_w \begin{pmatrix} \mathbf{0}^{4 \times 4} & \mathbf{0}^{4 \times 2} \\ \mathbf{0}^{2 \times 4} & \begin{matrix} C_D & -C_L \\ C_L & C_D \end{matrix} \end{pmatrix} \quad (7c)$$

where R_s Shell's equivalent radius when approximated as a sphere, A_x , A_y , and A_z are the cross-sectional areas of the body in the x-, y-, and z-axes directions, r is the radius of the cross-section, and $C_{(\cdot)}$ are empirical values of lift and drag coefficients estimated experimentally [1].

Added mass (\mathcal{M}_A) is an effect that arises when a body moves through a fluid, resulting from the fluid's inertia opposing the body's motion. The action of added mass is given by:

$$\mathcal{F}_A = -\mathcal{M}_A \dot{\eta}, \quad \bar{\mathcal{F}}_A = -\bar{\mathcal{M}}_A \dot{\eta}, \quad (8)$$

where $\dot{\boldsymbol{\eta}}$ is the screw acceleration twist. We compute the added mass on the shell of ZodiAq by assuming it to be a sphere submerged in infinite fluid. The simplified added mass of the shell \mathcal{M}_{Ashell} , shaft \mathcal{M}_{Ashaft} , hook $\overline{\mathcal{M}}_{Ah}$, and flagellum $\overline{\mathcal{M}}_{Af}$ are given by:

$$\mathcal{M}_{Ashell} = \rho_w V_{shell} \cdot \text{diag}[0, 0, 0, 0.5, 0.5, 0.5] \quad (9a)$$

$$\mathcal{M}_{Ashaft} = \rho_w V_{shaft} \cdot \text{diag}[0, 0, 0, 0, B_y, B_z] \quad (9b)$$

$$\overline{\mathcal{M}}_{Ah,f}(X) = \rho_w \pi r_{h,f}^2(X) \cdot \text{diag}[0, 0, 0, 0, B_y, B_z], \quad (9c)$$

where B_y and B_z are the added mass coefficients in the y and z axes. Since the force is linear with respect to $\dot{\boldsymbol{\eta}}$ (according to equation (2.2)), it essentially acts as adding a virtual mass to the body's mass. Hence, the generalized mass (\mathbf{M}) and Coriolis (\mathbf{C}) matrix are computed by incorporating the added mass of individual bodies. Meanwhile, all other external force components are projected into the generalized force vector \mathbf{F} .

After evaluating the terms in the equation (3), it is integrated in time using an ODE integrator to solve for $\mathbf{q}(t)$ and $\dot{\mathbf{q}}(t)$.

3 Creating ZodiAq's Digital Twin

SoRoSim (Soft Robot Simulator) is a Graphic User Interface (GUI) based MATLAB toolbox that can analyze open-, closed-, and branched hybrid robots under various external load and actuation scenarios [2]. We used the toolbox to create a digital twin of ZodiAq. This section documents the creation of the digital twin of the robot.

3.1 Defining Links and the Linkage

SoRoSim uses MATLAB class objects to model links (`SorosimLink`) and combine them to form linkages (`SorosimLinkage`). Links are the building blocks of any system modeled in SoRoSim and are categorized into two types: Soft and Rigid. The ZodiAq is a hybrid, branched linkage with 37 links that are classified into four `SorosimLink` class objects: Shell, Shaft, Hook and Flagellum. These links are created in SoRoSim by entering the appropriate material and geometric properties when prompted by the GUI. Table 1 outlines the geometric and material properties of each link.

Once these `SorosimLinks` are created, we combine them to create the linkage of ZodiAq. The reference frame of the Shell, located at its geometric center (GC), is aligned with the global frame. Since the joint of the shell was defined as a free joint during link creation, a corresponding basis function, as described in Section 2.1, is automatically assigned to it. After this, we incorporated the second link, the Shaft. We used a transformation matrix \mathbf{g}_f to accurately position and orient the Shaft relative to the Shell's reference frame. The value of \mathbf{g}_f depends on the face of the dodecahedron to which the shaft is assembled. After the assembly, we define the Shaft's basis function by specifying that the revolute joint rotates about the local x-axis of the Shaft's frame

Table 1: Geometric and material properties of links

Property	Shell*	Shaft	Hook	Flagellum
Link type	rigid	rigid	soft	soft
Base joint type	Free	Revolute	Fixed	Fixed
Radius (m)	-	0.002	0.0125	$0.0125 - 0.29X_i$
Length (m)	-	0.020	0.050	0.300
Density (kg/m^3)	-	7960	1062	1062
Elastic Modulus (N/m^2)	-	-	-	666190
Pisson's ratio	-	-	-	0.5
Material Damping ($Pa.s$)	-	-	-	11200

* Geometric and material properties of the shell are modified by a custom function.

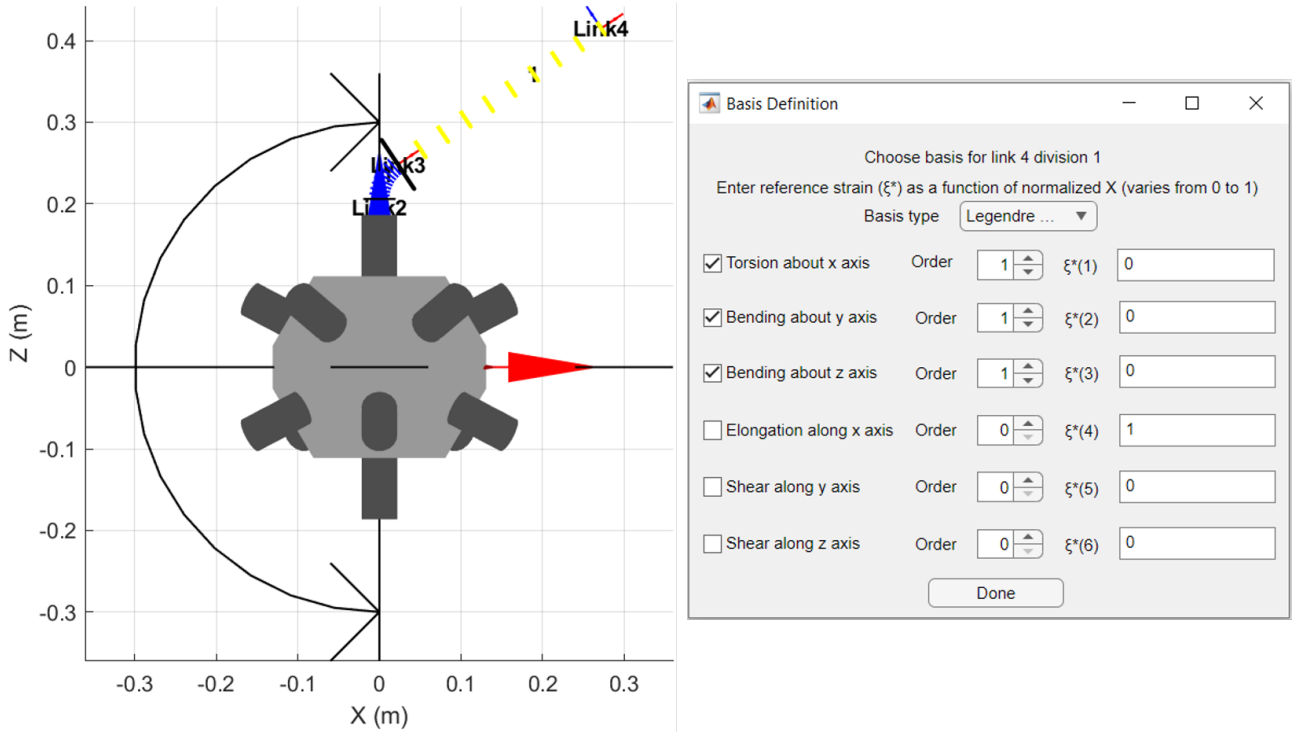


Figure 4: GUI showing the process of specifying the active modes of deformation and their order for a soft link

(Section 2.1). Following this, we assembled the Hook at the tip of the shaft. For the Hook we define a reference strain, $\xi_i^* = [0 \ \pi/(4l_h) \ 0 \ 1 \ 0 \ 0]^T$, where l_h is the length of the Hook. By assigning it with 0 DoF, we effectively model it as a curved rigid link. Finally, a flagellum is assembled at the tip of the Hook. The active modes of deformation of the Flagellum and their order are specified with the help of the GUI as shown in Figure 4. We activated torsion about the x-axis, along with bending about both the y-axis and the z-axis, with linear strain parameterization (1st order). This completes the assembly of the first branch. The same process is repeated 11 more times to assemble actuators on each face of the shell.

After completing the assembly, external forces and actuators are specified. Gravity is defined to be in the negative z-axis using the GUI. The revolute joints of all shafts are designated as actuators, controlled by joint angles. Following these specifications, the digital twin of ZodiAq is established as a **SorosimLinkage**. The change in mechanical properties due to the non-trivial shape of the Shell, the forces due to fluid interaction, and the control law are integrated into the system using separate MATLAB functions described in the next section.

3.2 Custom Properties, External Forces, and Actuation

Due to the arrangement of internal components, the GC and Centre of Mass (CM) of the Shell are not coincident, and the inertia matrix is not a diagonal matrix [1]. For ZodiAq, we estimated a vertical shift of $d_{CM} = 3.5\text{cm}$ between the GC and the CM. Based on the geometry of the dodecahedron and the motor canister assembly, the volume of the shell is calculated. Assuming neutral buoyancy, the mass is computed as $m = \rho_w V_{ext} = 8.57\text{kg}$. The moment of inertia of the dodecahedral shell about each axis is computed as follows:

$$I_x = I_y = \frac{ms^3(39\phi + 28)}{150} + md_{CM}^2, \quad I_z = \frac{ms^3(39\phi + 28)}{150}, \quad (10)$$

where $s = 0.1\text{m}$ is the edge length of the dodecahedron, ϕ is a constant equal to $\frac{1+\sqrt{5}}{2}$, and the term md_{CM}^2 comes from the parallel axis theorem to account for the vertical displacement of the CM. As the shift is along the z-axis, I_z remains unchanged. The updated inertia matrix \mathcal{M}_{shell} of the shell is given by:

$$\mathcal{M} = \begin{pmatrix} \mathcal{I} & m\tilde{\mathbf{c}} \\ -m\tilde{\mathbf{c}} & m\mathbf{I}_3 \end{pmatrix}, \quad (11)$$

where, $\mathcal{I} = \text{diag}[I_x, I_y, I_z]$, $\mathbf{c} = [0, 0, d_{CM}]^T$, and $\tilde{\mathbf{c}}$ denotes the skew-symmetric matrix form of the vector \mathbf{c} . A MATLAB file called `MoI_update.m` computes and updates the inertia matrix of the Shell.

SoRoSim employs a custom MATLAB script, `CustomExtForce.m`, allowing users to model various types of external forces. The toolbox accesses this file during the dynamic simulation if the `CEFP` (Custom External Force Present) property of the `SorosimLinkage` is enabled. We implement the models (Section 2.2) of buoyancy and drag-lift forces in this file (note that gravity is a default external force that can be enabled during linkage creation). We computed the drag-lift matrices (7) using a function called `DragLiftMatrix.m`, and saved the values as a custom property (`CP1`) of the `SorosimLinkage`. For the shell, we assume a spherical shell with a radius $R_s = 0.11\text{m}$ to simplify the calculations. By the same assumption, we have $A_x = A_y = A_z = \pi R_s^2$. The drag-lift coefficients used are as follows: $C_x = C_y = C_z = 2.5$ for the shell; $C_x = 0.01$, $C_y = C_z = 2.5$ for the shaft; $C_D = 1.1$, $C_L = -0.1$ for the hook; and $C_D = 1.1$, $C_L = -0.3$ for the filament. Similarly, the added mass (9) of each body is pre-computed using the file `AddedMass.m`, and the values are saved in the property called `M_added` of the `SorosimLinkage`. The added mass coefficients of the shaft are $B_y = B_z = 1.5$, while for the hook and flagellum, they are set to $B_y = B_z = 0.6$. As previously discussed, `M_added` is used for calculating the matrices \mathbf{M} and \mathbf{C} of equation (3).

The revolute joints of the shafts are actuated by joint angles, allowing users to specify actuation inputs as functions of time. The dynamic simulation is initiated by entering `ZodiAq.dynamics` in MATLAB's command window. Following this, the user can input joint angles as prompted by the GUI. Figure 2C in the manuscript illustrates the results of a dynamic simulation using an angle input of $2\pi t$ (60 RPM) for motors M6, M8, M9, and M11, while setting 0 for the remaining motors. Another method for specifying actuation involves utilizing the `CustomActuatorStrength.m` file. Initially, one must enable the `CAS` (Custom Actuation Strength) property

of the `SorosimLinkage` by entering `ZodiAq.CAS=true` in the MATLAB command window. Subsequently, the file can be modified to define the actuation inputs. We used this file to implement a control law for ZodiAq's navigation. The implemented control law is described in the next section. Interested readers can simulate the digital twin in MATLAB using the SoRoSim files available at the GitHub link provided in [3].

4 Control Design for Robot Navigation

In this section, we present a simplified model to develop the motion control of the robot for performing navigation. This model is essentially obtained by representing the system as a solid body evolving in 3D and subject to the forces and moments generated by the rotation of the motors at the centre of each face (see Figure 6).

4.1 Simplified Dynamic Model

The simplified dynamic model used for the development of the control law is derived under the following assumptions:

- The main structure of the robot is supposed to be rigid.
- The structure is supposed to be symmetrical respect to its vertical axis.
- The system mainly rotates only around its vertical axis due to its inherent stability by design (CM is below the center of buoyancy), permitting significant rotations solely around this axis. As a result, small angle approximations have been employed for the other two angles.
- We assume perfect neutral buoyancy of the system, the effect of the gravity and buoyancy can be neglected.
- The flagellum rotation generates a thrust and an angular moment which are proportional to the flagellum's speed and they are perpendicular to its face.
- All flagella are equal, meaning that each of these appendages shares identical properties, such as length, material composition, and structural characteristics.

As the motor rotates, the soft flagella interact with the surrounding fluid and deform, resembling an helical shape that depends of many parameters, including the stiffness of the material and the rotational speed of the motor. This interaction generates forces and torques exerted during the rotation of the flagella. In total, three torques (m_x , m_y and m_z) and three forces (f_x , f_y and f_z) are produced. The results presented in [1] showed that only two reaction forces are not null, on average, during the rotation of a single flagellum: the propulsive thrust f_x and the out-of-plane torque m_x . We simulated the rotation of the flagellum at different angular velocities using our toolbox SoroSim to obtain the reaction forces and moments at the base generated by the rotation. The angular velocity range $[0 - 4]\pi$ rad/s was chosen to align with the operational capabilities of the selected motors inside the water. Figure 5A and Figure 5B show the reaction forces for a rotation speed of π rad/s. We observe that only the propulsive thrust f_x and the out-of-plane torque m_x are not null during

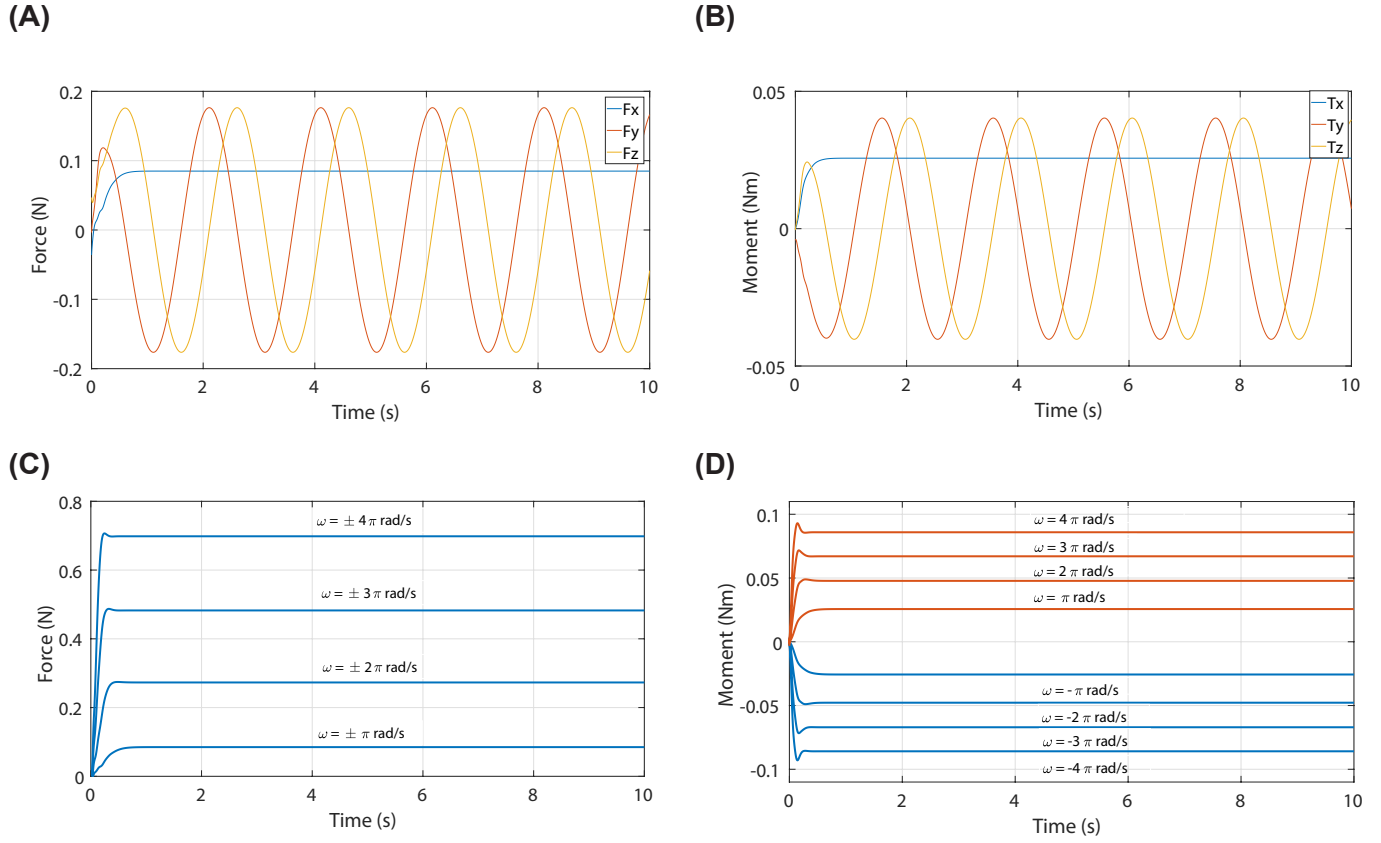


Figure 5: Constraint torques and forces exerted at the base of the flagella, obtained from the theoretical simulations at different speeds. It can be noticed that only the propulsive thrust f_x and the out-of-plane torque m_x have a nonzero mean.

the rotation, matching the results obtained in [1]. Figure 5C and Figure 5D represent f_x and m_x for different angular velocities. Considering the steady state values of the functions and the range of actuation of the motors, the reaction forces are approximated as first-order functions of the angular speed. Specifically, propulsive thrust is approximated as $f_x = a_1 \cdot |\omega|$, and the moment is approximated as $m_x = a_2 \cdot \omega$ being $a_1 = 0.065$ and $a_2 = 0.0064$.

The rotation of a rigid body in space can be parameterized using the well-known Euler angles. Then, the complete rotation matrix is the product of the three successive rotations $\mathbf{R}(\phi, \theta, \psi) \in SO(3)$. Assuming small angles in ϕ and θ , we have that $\mathbf{R}(\phi, \theta, \psi) \approx \mathbf{R}(\psi)$. The rotation dynamics is modelled using Euler-Lagrange Formalism.

$$\Gamma_i = \frac{d}{dt} \left(\frac{\delta L}{\delta \dot{q}_i} \right) - \frac{\delta L}{\delta q_i} \quad (12)$$

Let us consider earth fixed frame E , body fixed frame B and the frames of the faces C_i as seen in Figure 6A. In this simplified model, we position the origin of the body-fixed frame at the CM of the system. The airframe orientation in space is given by a rotation $\mathbf{R}(\psi)$ from B to E . The mechanical symmetry of the system allows us to neglect the inertia products and consider a diagonal inertia matrix. The three equations that describe the dynamics of the rotations are:

$$\begin{bmatrix} I_x \ddot{\phi} \\ I_y \ddot{\theta} \\ I_z \ddot{\psi} \end{bmatrix} = \begin{bmatrix} \dot{\theta} \dot{\psi} (I_y - I_z) \\ \dot{\phi} \dot{\psi} (I_z - I_x) \\ \dot{\phi} \dot{\theta} (I_x - I_y) \end{bmatrix} + \begin{bmatrix} \tau_\phi \\ \tau_\theta \\ \tau_\psi \end{bmatrix} \quad (13)$$

The detailed mathematical derivation of (13) is provided in Appendix B.2 of [4]). Conversely, the dynamics of the translations are developed using Newton-Euler Formalism:

$$m \begin{bmatrix} \ddot{x} \\ \ddot{y} \\ \ddot{z} \end{bmatrix} = \mathbf{R}(\psi) \begin{bmatrix} f_x \\ f_y \\ f_z \end{bmatrix} \quad (14)$$

where x , y and z are the position in the earth fixed frame E. Then, we can express equations (13) and (14) in the following matrixial form:

$$\mathbf{M} \ddot{\mathbf{q}} + \mathbf{C}(\mathbf{q}, \dot{\mathbf{q}}) \dot{\mathbf{q}} = \mathbf{u} \quad (15)$$

where

$$\boldsymbol{\Upsilon} = \begin{bmatrix} \mathbf{I}_{3 \times 3} & \mathbf{0}_{3 \times 3} \\ \mathbf{0}_{3 \times 3} & \mathbf{R} \end{bmatrix}$$

and $\mathbf{q} = [\phi, \theta, \psi, x, y, z]^T$ is the vector of generalized coordinates of the simplified system, \mathbf{M} is the inertia matrix, $\mathbf{C}(\mathbf{q}, \dot{\mathbf{q}})$ is the generalized Coriolis matrix and \mathbf{u} is the generalized forces. Assuming small angles in θ and ϕ , the generalized forces projected in the Euler angles can be approximated as resultant force and moment applied to the CM of the robot. Following this, the forces produced by the rotation of the 12 flagella can be expressed as:

$$\mathbf{F}_G = \sum_{i=1}^{12} \mathbf{F}_i; \quad \mathbf{M}_G = \sum_{i=1}^{12} (\mathbf{M}_i + \mathbf{r}_{G,i} \times \mathbf{F}_i); \quad (16)$$

We can establish the reference frame, C_i , linked to face i by using the rotation matrix \mathbf{R}_{fi} . Then, the forces and moments generated at each face can be expressed in the frame of the rigid body as $\mathbf{F}_i(\omega_i) = \mathbf{R}_{fi}[-a_1 \cdot |\omega_i|, 0, 0]^T$ and $\mathbf{M}_i(\omega_i) = \mathbf{R}_{fi}[-a_2 \cdot \omega_i, 0, 0]^T$. We establish a fixed rotation direction for each flagellum; then, the absolute module can be removed, simplifying the control law and optimizing the system's performance. We choose that the flagella in the 1, 2, 5, 6, 9, 10, faces rotate counter-clockwise, while the remaining ones rotate clockwise. This deliberate choice aims to neutralize aerodynamic torques during stable and straight maneuvers (see Figure 6B). Then, the forces and moments can be expressed as follows:

$$\mathbf{F}_i(\omega_i) = \mathbf{r}_i \cdot \omega_i; \quad \mathbf{M}_i(\omega_i) = \mathbf{p}_i \cdot \omega_i \quad (17)$$

where

$$\mathbf{r}_i(\omega_i) = \mathbf{R}_{fi}[-a_1, 0, 0]^T; \quad \forall i \quad (18)$$

$$\mathbf{p}_i(\omega_i) = \begin{cases} \mathbf{R}_{fi}[-a_2, 0, 0]^T & \forall i = 1, 2, 5, 6, 9, 10 \\ \mathbf{R}_{fi}[+a_2, 0, 0]^T & \forall i = 3, 4, 7, 8, 11, 12 \end{cases} \quad (19)$$

Expressions (17) can be simplified as follows:

$$\mathbf{M}_G = \sum_{i=1}^6 \underbrace{(\mathbf{p}_{k(i)} + \mathbf{r}_{G,k(i)} \times \mathbf{r}_{k(i)})}_{\mathbf{s}_{k(i)}} \underbrace{(\omega_{k(i)} - \omega_{k(i)+1})}_{\Omega_i}; \quad \mathbf{F}_G = \sum_{i=1}^6 \mathbf{r}_{k(i)} \underbrace{(\omega_{k(i)} - \omega_{k(i)+1})}_{\Omega_i}; \quad (20)$$

where $k(i) = (i-1) \cdot 2 + 1$, $\mathbf{r}_i = -\mathbf{r}_{i+1}$, $\mathbf{p}_i = -\mathbf{p}_{i+1}$ and $\mathbf{r}_{Gi} \times \mathbf{r}_i = -\mathbf{r}_{G,i+1} \times \mathbf{r}_{i+1}$ due to the symmetry of the system (see Figure 6A). Therefore, the resultant forces and moments applied to the CM, using the new control input $\boldsymbol{\Omega} = [\Omega_1, \Omega_2, \dots, \Omega_6]^T$, can be represented in matrix form as follows:

$$\mathcal{F}_G = [\mathbf{M}_G^T, \mathbf{F}_G^T]^T = \boldsymbol{\Xi}(\Theta) \cdot \boldsymbol{\Omega} \quad (21)$$

where $\boldsymbol{\Xi}(\Theta) \in \mathbb{R}^{6 \times 6}$ is a constant matrix whose columns are $[\mathbf{s}_{k(i)}^T, \mathbf{r}_{k(i)}^T]^T$. Additionally, we incorporate the effects of the fluid on the body through the term $\mathbf{F}(\mathbf{q}, \dot{\mathbf{q}})$, which encompasses gravitational forces and fluid-body interactions including buoyancy, drag, lift, and added mass. The details of $\mathbf{F}(\mathbf{q}, \dot{\mathbf{q}})$ for the rigid body are described in Section 2.1 for the shell of the system. Consequently, the simplified dynamic equation can be formulated as follows:

$$\mathbf{M}\ddot{\mathbf{q}} + \underbrace{\mathbf{C}(\mathbf{q}, \dot{\mathbf{q}})\dot{\mathbf{q}} - \mathbf{F}(\mathbf{q}, \dot{\mathbf{q}})}_{\boldsymbol{\zeta}(\mathbf{q}, \dot{\mathbf{q}})} = \boldsymbol{\Upsilon}(\boldsymbol{\psi}) \cdot \boldsymbol{\Xi}(\Theta) \cdot \boldsymbol{\Omega} \quad (22)$$

Remark 1. The rotation direction of each flagellum remains unchanged in the predefined configuration because any alteration does not impact the direction of the thrust; it only affects the moment's direction. This assumption simplifies the control law by removing the absolute value in the thrust function.

Remark 2. The magnitude of the angular speed, denoted by ω_i , is inherently positive. Conversely, the new control input Ω_i can assume any real value. To generate a positive Ω_i , ω_i is actuated while keeping ω_{i+1} zero. On the contrary, to generate a negative Ω_i , ω_i is kept zero, and ω_{i+1} is actuated.

4.2 Control law

In this section we will develop a control strategy for controlling the position and orientation $\boldsymbol{\psi}$ of the system, provided that the generalized coordinates of the system associated with the main body, \mathbf{q} , and its derivatives are known. As the orientation angles ϕ and θ exhibit inherent stability by design, we abstain from direct control of these variables. This allows us to streamline the control technique, enhancing computational efficiency. Consider the nonlinear system described in (22), we can control the coordinates $\bar{\mathbf{q}} = [\boldsymbol{\psi}, x, y, z]^T$ by taking the four last

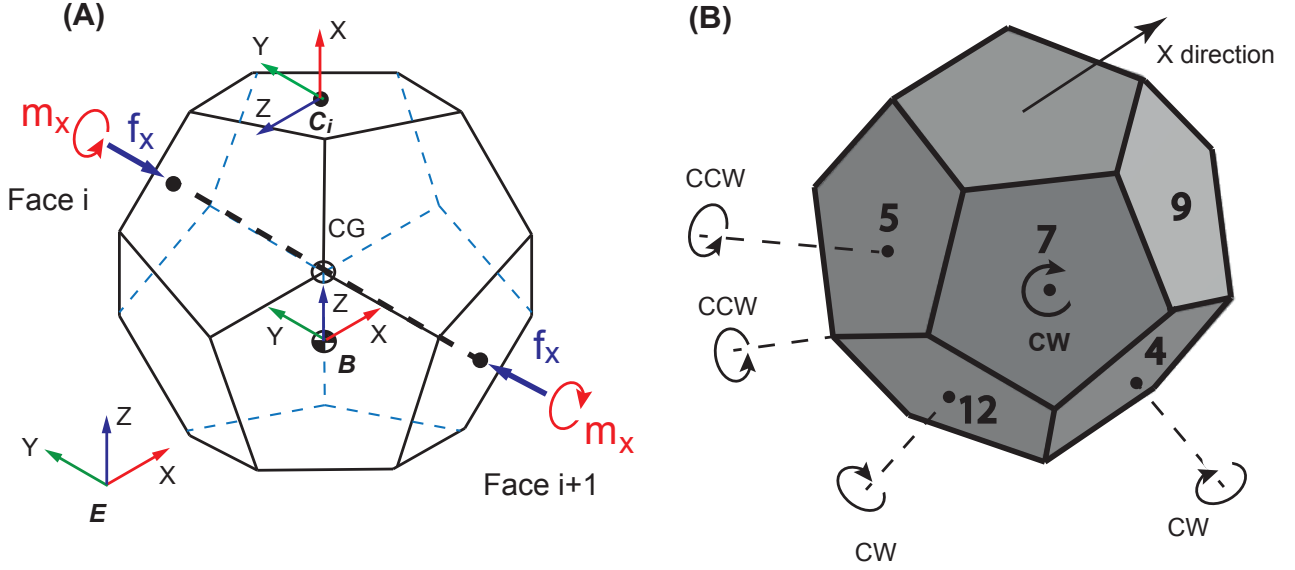


Figure 6: Zodiac main body representation: (A) Representation of the different frames and exerted forces/moments acting on the robot. (B) Indication of rotational directions for each flagellum.

equations which correspond with those coordinates as follows:

$$\Omega = (\bar{\Upsilon} \cdot \bar{\Xi}(\Theta))^\dagger \cdot (v + \bar{\zeta}(q, \dot{q})) \quad (23)$$

where we denote the pseudo-inverse of a matrix as $(\bullet)^\dagger$, and let v be a new input that cancels the nonlinearities, thereby transforming the system into:

$$\bar{M} \cdot \ddot{q} = v \quad (24)$$

The design of a tracking controller for this double-integrator relation can be easily obtained through a proportional-derivative (PD) controller as follows:

$$v = \bar{M}(\ddot{q}^* - K_d(\dot{q} - \dot{q}^*) - K_p(q - q^*)), \quad (25)$$

with K_d and K_p being positive constants, the tracking error of the closed loop system is exponentially stable.

Remark 1 and 2 enable the elimination of the absolute value in the thrust function, facilitating the definition of the new control input Ω . This simplifies the control law and guarantees that the system (22) becomes differentially flat.

4.3 Controller implementation for experimental tests

As our experimental setup lacks a tracking system, we are unable to provide feedback on planar coordinates (x and y) for the real prototype. To accommodate this limitation, we have made slight modifications to the control law (23)-(25) to enable the execution of various trajectories with the system. We make the assumption that the term $\bar{\zeta}(q, \dot{q})$ is negligible due to the system's slow velocity. Moreover, we implement closed-loop control for the

depth and orientation about the vertical axis (ψ). Meanwhile, the planar movement (x and y) was controlled in an open-loop manner by commanding a desired acceleration $\ddot{\mathbf{q}}^*$. As a result, the control law can be simplified to:

$$\mathbf{\Omega} = (\overline{\mathbf{r}} \cdot \overline{\mathbf{\Xi}}(\Theta))^{\dagger} \cdot \overline{\mathbf{M}} \cdot \begin{pmatrix} \ddot{\psi}^* - K_d(\dot{\psi} - \dot{\psi}^*) - K_p(\psi - \psi^*) \\ \ddot{x}^* \\ \ddot{y}^* \\ \ddot{z}^* - K_d(\dot{z} - \dot{z}^*) - K_p(z - z^*) \end{pmatrix}; \quad (26)$$

References

- [1] Armanini C, Farman M, Calisti M, Giorgio-Serchi F, Stefanini C, Renda F. Flagellate Underwater Robotics at Macroscale: Design, Modeling, and Characterization. *IEEE Transactions on Robotics*. 2022;38(2):731-47.
- [2] Mathew AT, Hmida IMB, Armanini C, Boyer F, Renda F. SoRoSim: A MATLAB Toolbox for Hybrid Rigid-Soft Robots Based on the Geometric Variable-Strain Approach. *IEEE Robotics and Automation Magazine*. 2022.
- [3] Ben Hmida I, Feliu-Talegon D, Mathew AT. ZodiAq digital twin in SoRoSim: ZodiAq Branch; 2023. GitHub repository, ZodiAq branch. Available from: <https://github.com/Ikhlaz-Ben-Hmida/SoRoSim/tree/ZodiAq>.
- [4] Samir B. Design and control of quadrotors with application to autonomous flying. Project report, Ecole Polytechnic. 2007.